Soft X-ray Spectroscopic Investigation of Oxides for Renewable Energy Applications

Senior Thesis
May 2012
Chancellor's Honors Program

Eric W. Martin
Engineering Physics
The University of Tennessee, Knoxville

Dr. Norman Mannella, Research Advisor

ACKNOWLEDGEMENTS

At the University of Tennessee I have been able to more than maximize my potential in these four short years of college. The Physics Department, specifically, has provided tremendous support and advice throughout my undergraduate career. The faculty has supplied a comprehensive course load, a plethora of research opportunities, and even resources for side projects upon request. In particular, Dr. James Parks, Dr. Marianne Breinig, and Dr. Geoff Greene have been tremendous influences. They have opened many doors for me and exposed me to the most incredible of the world's topics through, of course, physics.

The Chancellor's Honors Program has certainly enhanced my experience at the University of Tennessee. It has provided benefits that permitted me the freedom to build a solid education that has prepared me for experimental physics research and graduate course work. The Honors Program also deserves my thanks for awarding me a Research Grant that helped allow me to collect some of this project's data at the Advanced Light Source at the Lawrence-Berkeley National Lab.

For both the development of this project and my own development, a big thanks goes out to Drs. Paolo Vilmercati and Christine Cheney. I have been very lucky to be able to work so closely with two knowledgeable researchers who have cared to see me learn. Over the past couple years these mentoring relationships have turned additionally into friendships, and I am very glad for that.

As for my advisor Dr. Norman Mannella, I could not have had such a fantastic and educational experience without his enthusiastic help and encouragement. He has given me an unbelievable amount of his time, expertise, and care. Norman has sent me to the ALS to collect data, sent me to Dallas to present my research, trusted me to work in a most advanced condensed matter research lab, taught me courses worth of material to supplement my physics education, and all the while he has treated me as an equal. I really cannot envision a better advisor.

ABSTRACT

Oxide materials with potential applications as interfaces with renewable energy sources have been studied using several soft x-ray spectroscopic techniques. Given society's high demand for energy and earth's rapidly depleting fossil fuel sources, the relevance of oxide materials for energy is evident, particularly given the stability of oxides in air. In this project, the study of two such materials is detailed. Along with presenting the important conclusions of the research projects, the versatility of photoemission spectroscopy (PES) is highlighted as an invaluable technique for the condensed matter study of materials for energy.

Titanium dioxide (TiO_2) is known for its photovoltaic properties (its ability to convert photon energy into electricity), but the parent compound's electronic structure does not permit it to absorb photons with low enough energies to be in the visible spectrum. Nitrogen doping has been shown to increase the absorption of more light in the visible spectrum, and thus lead to a higher efficiency for solar applications. The problem is getting N to be successfully substituted for oxygen in the doped compound. In this project, one proposed solution has been experimentally tested using the dependence of photoemission measurements on composition density. The data offer conclusive evidence that codoping TiO_2 with N and Cr does encourage the absorption of N. However, the data suggest that the contributions of the two dopants differ from those that were proposed.

Magnesium-doped rhodium oxides with formula unit $CuRh_{1-x}Mg_xO_2$ and delafossite-type structure were recently found to exhibit a high thermoelectric figure of merit at high temperatures. Soft x-ray spectroscopic techniques have been used to characterize the electronic structure of the Rh-oxides at the Fermi edge. Inspiration for the project arose from the delafossite-type cobalt based oxides that also exhibit high thermoelectric properties at high temperatures. X-ray emission (XES) and PES spectra taken at synchrotrons have provided solid experimental evidence that the thermoelectric properties of thermoelectric oxide materials stem from the orbital degrees of freedom of the low spin d^6 Co and Rh ions. Analysis of the Rh-oxide data has provided a complete determination of the densities of states of Cu and Rh at the Fermi level. The topology of the states rooted in transport has also been revealed by the strong dependence of rhodium's signal in single crystal samples on light source polarization.

TABLE OF CONTENTS

LIST OF TABLES

Table Page

LIST OF FIGURES

Figure Page

CHAPTER I
INTRODUCTION AND GENERAL INFORMATION

Fundamental Purpose

With a rising demand for energy and a falling supply of the world's finite reserves of fossil fuels, the pursuit of alternate forms of energy is currently driving scientific research. Solar and thermal energy are two of the most abundant natural sources, so their efficient capture is of utmost importance. The solar market has been primarily driven by silicon solar cells, and geothermal power is currently still most efficiently captured by a steam engine. Though these are the most affordable options, silicon solar cells are limited by the theoretical maximum absorption of 29% of impinging sunlight and steam engines are known to be have about 20% Carnot Efficiency.[1] It is therefore imperative that new interfaces between societal needs and finite natural energy supplies be found. This necessity brings to the forefront the role of advanced materials for production, transport and storage of energy. Materials for energy applications additionally demand stability in air at elevated temperatures. Oxide materials meet these criteria, and thus they are an intuitive starting point for renewable energy endeavors.

The design of new materials for energy applications requires a sound understanding of their macroscopic, and ultimately microscopic properties. Attaining a correct description of their electronic structures is one of the most essential steps.

In this project, the primary traits of the electronic structures of two prototypical materials for energy applications have been studied by means of a unique combination of spectroscopic

techniques in the soft x-ray regime. This project will describe in detail the original conclusions regarding photocatalytic Titanium Dioxides (TiO_2) and Rhodium based oxide thermoelectrics.

Photovoltaic Effect and TiO_2

The generation of affordable and environmentally clean energy from a sustainable source is one of the greatest dreams of society. As one of the most abundant sources of energy accessible from earth is the sun, the efficient capture of solar energy is arguably one of the greatest chances for society to escape its reliance on fossil fuels. To utilize solar energy one must either convert it to thermal energy by an interface's absorption of infrared rays, or one may use a photovoltaic material to directly generation current by the absorption of photons.

Photovoltaic materials exploit the photoelectric effect (described in more detail in Chapter II). The photoelectric effect describes an atom's absorption of a photon with a quantized amount of energy that leads to the excitation of an electron into a higher energy state. When applied to photovoltaics, this excitation is typically of an electron in the valence band (the occupied electron states in the outermost electron shell of an atom) to the conduction band. A potential difference is applied across these materials so that the excited electron begins to move before recombining with the hole that has been created in the valence band (VB). There are a few important issues that follow directly from these points:

1) Photons can only excite electrons that are bound by an energy that is less that the energy of the photon. The energy required to excite an electron in the VB to the conduction band (CB) is equal to the energy difference between those two bands, which is generally

referred to as the band gap. The energy distribution of the sun depicted in Figure 1 may be used to determine ideal band gaps for absorption of light from the sun.

2) The photoelectric effect is not the only process that can occur when light interacts with matter, if the light interacts with the material at all. For this reason, the atoms that contribute electrons to the conduction band in the most ideal photovoltaics have large photoemission cross-sections. Typically this is correlated to the photovoltaic efficiency.

3) Current must be able to flow in these materials to both generate power and minimize the likelihood of the excited electrons' recombination with their corresponding VB holes. Ideal materials thus cannot be insulating and must have what is called a high charge carrier mobility.

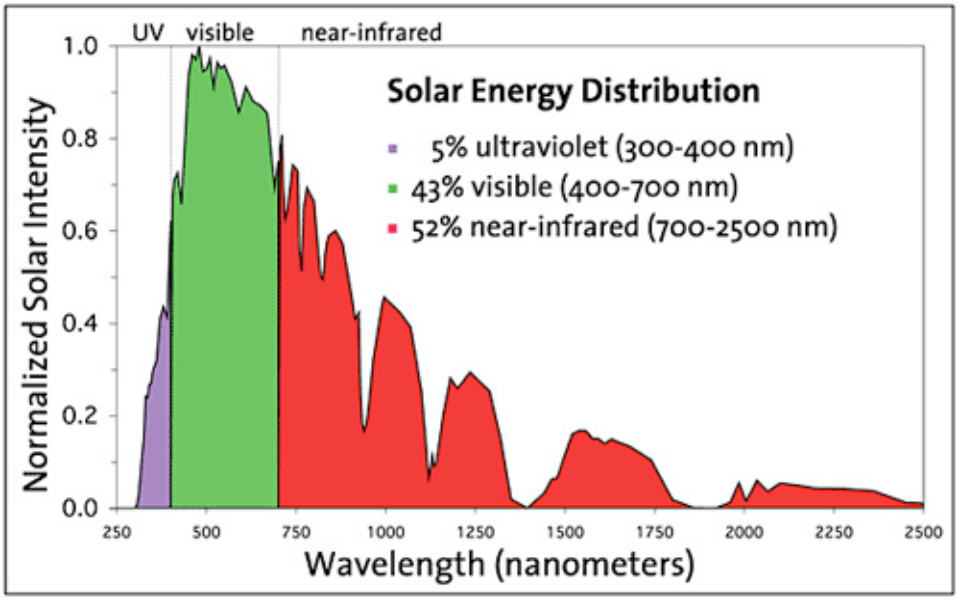

Figure 1. Solar intensity as a function of photon wavelength to show the energy ranges to which pholtaics should be tuned.[2]

In the early 1970s, Fujishima and Honda showed that water can be split into H_2 and O_2 by using a TiO_2 photocatalyst. Though known for its propensity to assist in the catalysis of water,

this photocatalyst may be applied to other solar energy generation processes due to the high propensity of light to excite electrons in TiO_2. Furthermore, TiO_2 is stable against corrosion in the electrolyte of a fuel cell. Particularly given that it is an oxide, one may expect such stability in many environments. For these reasons TiO_2 is considered one of the more promising materials for solar energy generation.[3,4,5]

The weakness of TiO_2 is that its intrinsic bandgap is 3.2eV, which corresponds to the absorption of photons with wavelengths that are less than 390nm. From Figure 1 it is evident that this ultraviolet region of the solar spectrum has a very low intensity, and thus the bandgap of TiO_2 has to be decreased for application to solar energy generation.[6] In 2001, Asahi determined that the introduction of nitrogen (N) into TiO_2 (called doping) decreases the cutoff frequency to a corresponding wavelength of 500nm.[7] The mechanism for this is not entirely understood, but the most well supported theory argues that N introduces occupied states between the VB and CB that allow electrons to jump from the VB to CB in two lower energy steps as depicted in Figure 2.

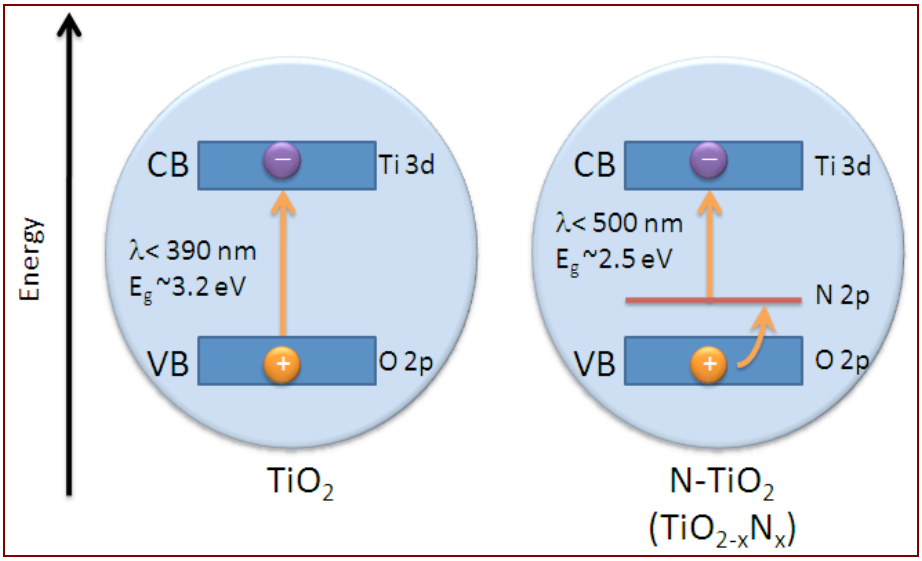

Figure 2. Diagram of bandgaps of undoped and N doped TiO2 as theorized by Nakoto and Irie.[8]

The difficulty with N doping is that N is not very soluble in TiO_2. This has been true for most doping schemes in which the majority of the dopant atoms reside at interstitial sites in the materials.[9] The purpose of the experiment presented in Chapter V has thus been to study new doping schemes that are believed to more effectively lead to the TiO_2 absorption of substitutional N. Not only does this experiment serve to provide insight into the structure of doped TiO_2, but it aids in the characterization of a new doping scheme. Developing an understanding of how to control the electronic band structure of a host material is a pursuit that, if ever successful, will drive innovative materials science over a much wider spectrum of topics than TiO_2 photovoltaics alone.

Thermoelectricity and $CuRh_{1-x}Mg_xO_2$

The thermoelectric effect is a process by which a thermal gradient is used to induce an electric potential difference over a material and vice versa. The movement of charge due to a difference in temperature is known as the Seebeck Effect and is of great interest due to its application to energy research. The reverse process by which a current through a material can be used to cool the material is known as the Peltier Effect.

Materials' propensities to exhibit this effect are compared by a calculable figure of merit. Maximization of this figure requires a high Seebeck coefficient, a value relating the voltage potential difference induced to the temperature difference ($S_{TEP} \equiv -\frac{\Delta V}{\Delta T}$). The figure of merit (Z) is also inversely proportional to electrical resistivity (ρ) and thermal conductivity (κ). The logic behind the definition of the figure of merit originates with the definition of power ($P = IV$). As both voltage and current are related linearly to power, doubling one is equivalent to doubling the

other. Therefore an appropriate figure of merit should relate the two equally. The voltage induced in a thermoelectric is defined entirely by the Seebeck coefficient, the temperature dependent relation of voltage and temperature S_{TEP}. Current has a linear relation to resistance ($I = \frac{V}{R}$), and from this arises its inverse proportionality to resistivity. Maintaining the flow of electrical current over the thermal gradient requires a thermal disequilibrium. Just as charge flows, phonon movement is induced by a thermal disequilibrium and can decrease the thermal gradient. For this reason the flow of electrons is also inversely proportional to thermal conductivity. Given the linear relationship of voltage and current to power, the appropriate figure of merit takes the form:

$$ZT \equiv \frac{S_{TEP}^2}{\rho \kappa} T$$

The focus of this project is $CuRhO_2$ primarily to understand the reason for its high S_{TEP}. It is generally understood that the entropy of the charge carrier distribution determines thermopower. In Co oxides spin and orbital entropy is maximized by the degeneracies of the Co^{3+} and the Co^{4+} orbital states. The interplay between the crystalline field and Hund's rule coupling leads to the degeneracy in the electronic states of Co ions. The degeneracy manifests itself as a

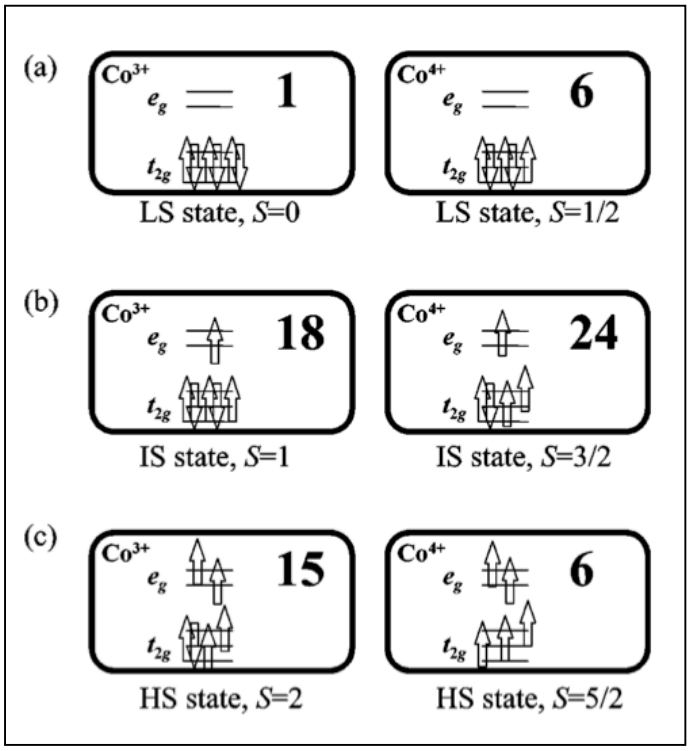

Figure 3. Spin and orbital degeneracies of Co3+ and Co4+ ions are given for (a) low-spin, (b) intermediate-spin, and (c) high-spin states. Lines indicate energy levels and arrows represent an electron's spin.[10]

splitting into e_g and t_{2g} energy levels. The occupation of these levels defines the low, intermediate, and high spin states depicted in Figure 3.[10] In Rh oxides, Rh^{3+} and Rh^{4+} orbital states have the same degeneracies and should thus enhance thermopower in the same manner.[11,12] Additionally, the Rh valence band is comprised of electron states in the 4*d* orbital, and so Rh oxides are expected to have a wider band width than the 3*d* Cu band.

As expected, $CuRhO_2$ exhibits exceptionally high S_{TEP} values. However, this parent compound is a band insulator, which means it has a high resistivity and consequently a low thermoelectric figure of merit. Upon doping with magnesium (Mg), where Rh^{3+} is substituted with Mg^{2+}, the oxide undergoes an insulator to metal transition and becomes conductive.[13] Despite the decrease in thermopower upon doping, the power factor ($\equiv S_{TEP}^2/\rho$) of polycrystalline $CuRh_{0.9}Mg_{0.1}O_2$ is actually almost twice that of polycrystalline Na_xCoO_2 over a wide range of temperatures.[14] The doping dependence of $CuRh_{1-x}Mg_xO_2$ is depicted in Figure 4 in addition to the compound stability as a function of temperature.

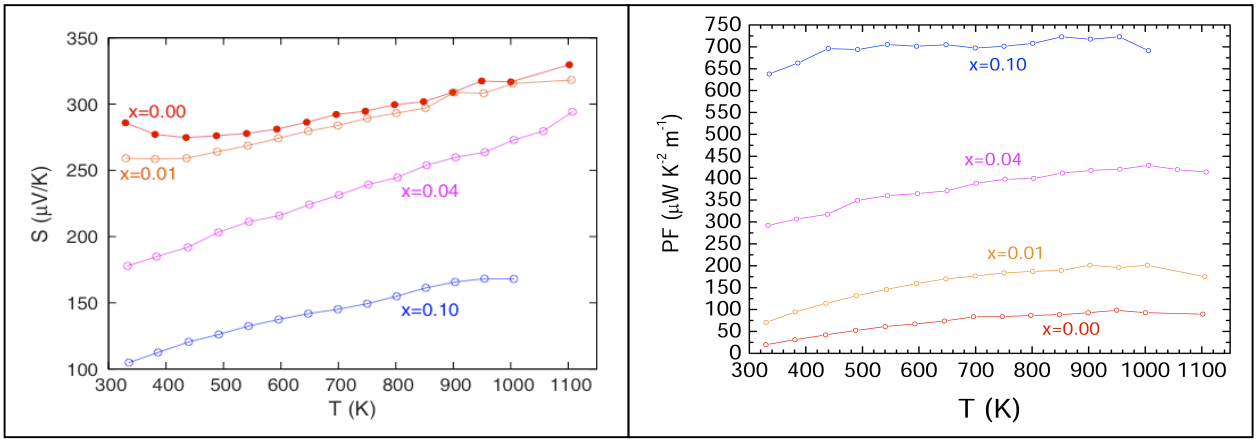

Figure 4. Temperature dependence of thermopower (*S*) and the power factor (PF) of $CuRh_{1-x}Mg_xO_2$ for x = 0, 0.01, 0.04, and 0.10.[13]

Given its impressive characteristics as a high temperature thermoelectric oxide, $CuRh_{0.9}Mg_{0.1}O_2$ is a valuable material worth studying as a prototype for an ideal thermoelectric

material for real world application. For the development of a microscopic description of thermopower, the study of Rh based oxides may be even more. Since the valence electronic structure of Rh is so similar to Co, and since both seem to be at the heart of thermoelectric transition metal oxides, the details of these materials' electronic structures most likely hold the secrets of thermopower in oxides.

CHAPTER II

SPECTROSCOPIC TECHNIQUES

Introduction

The measurement and understanding of microscopic electronic structures requires a very advanced set of tools. This chapter will describe the fundamentals of some of these techniques and the motivation for their use in these projects.

Photoemission Spectroscopy (PES)

History

In 1887, Heinrich Hertz found that he could lower the voltage required to create a spark between electrodes by shining ultraviolet light on the metal electrodes. This was the first observation of the photoelectric effect. In 1905, Albert Einstein provided the first theoretical description of the photoelectric effect in which quantized photons with energies greater than the attraction energy of electrons bound in a metallic lattice could excite those electrons. Furthermore, if the energy of the photon ($h\nu$) is greater the binding energy (BE) of the excited electron, the electron is ejected from the sample with a kinetic energy equal to the difference between the $h\nu$ and BE. Initial experiments only measured electrons bound to metallic lattices, primarily since ultraviolet energies are not great enough to excite more tightly bound electrons.[15] In 1907, after Wilhelm Röntgen's discovery and study of x-rays, much higher energy photons were used to excite electrons. These electrons were measured as a function of their velocities by

applying magnetic fields to the emitted electrons and detecting them with photographic plates. Since these x-rays were not monochromatic and the data not well understood, spectroscopic investigations of atomic structure were distant, but these experiments again confirmed that the energies of the emitted electrons are independent of the intensity of light used to excite them. In the 1950s, Kai Siegbahn began publishing the first high-resolution x-ray photoelectron spectroscopy (XPS) data.[15] In the mid-1960s, XPS was named electron spectroscopy for chemical analysis (ESCA) for its application to the study of the electronic structure of atoms and their chemical shifts in compounds.[16]

Fundamental PES

The PES technique utilizes the photoelectric effect to measure the binding energies of electrons in a sample. Surfaces are irradiated with monochromatic light, electrons are excited out of the sample by the photoelectric effect, and electron analyzers measure the photoelectrons as a function of their kinetic energies (KE). The KE of photoelectrons are given by:

$$KE = h\nu - BE - \Phi_s, \qquad (1)$$

where Φ_s is the spectrometer work function. The binding energy (BE) is defined as the energy difference between the initial and final states. The final energy for photoemitted electrons is 0, which corresponds to the Fermi level, E_F.

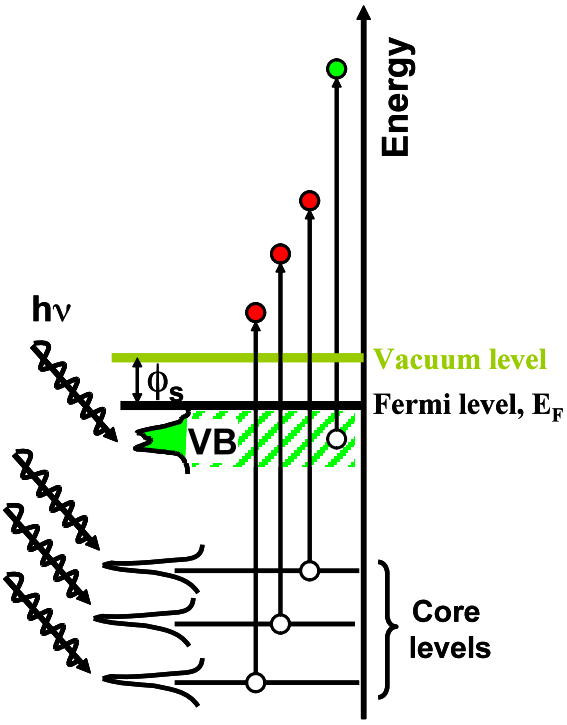

Figure 5. Diagram illustrating the photoelectric excitation of valence band (VB) and core level electrons by photons with energy *hν*.[17]

The frequently referenced components of these spectra are E_F, the valence band (VB), and the core levels. The electrons with states at E_F are the least bound electrons in a metal and the electrons that contribute to conduction. The VB in a spectrum corresponds to the electrons in the outermost orbital of each atom in the measured sample. These are the electrons involved in the bonds between atoms. Lastly, the core level electrons are the more tightly bound electrons in filled electron orbitals. Though these electrons' energies can be chemical shifted by some chemical environments, their binding energies are generally fairly stable. For this reason, a core level electron spectrum can generally function as a good fingerprint of an atom.

PES is a powerful technique with applications ranging from chemical composition determination to direct study of the interactions of electrons in materials. The measured spectra using PES have dependencies on the component densities, the energies of the photons used to excite the spectra, and the physical depth of the measured electrons (see Chapter IV for a more comprehensive discussion of photoemission dependencies and their analysis). Exploitation of these factors opens many doors for the study of electronic structures.

Special Techniques

Since PES measurements are not elementally sensitive, it is not always easy to resolve electron states with overlapping energies. This is particularly a problem in the VB where all photoelectrons from the outermost orbitals of all the constituent atoms are emitted with kinetic energies in a small range of about 10eV. Several techniques have thus been designed to distinguish electron states.

One method of distinguishing features is to exploit the dependence of those features' intensities on the photoemission cross sections of their respective orbitals. These cross sections

can be calculated for each orbital and have a dependence on the energy of the excitation photon. To perform these measurements, a tunable photon source is used to excite PES spectra with a range of photon energies. If a range of energies is selected over which the measured orbitals have differing cross section dependencies, the spectral weights of the PES features will change. Each spectral weight should follow the trend of its corresponding cross section dependence. For a thorough application of this technique, see Chapter VI as the technique is applied to the determination of the electron structure of $CuRh_{1-x}Mg_xO_2$.

The propensity to excite a directional covalent bond is dependent on the polarization of the excitation photon. The reason for this is that a changing electric field oriented in the direction of the bond will resonate that bond, but a field oscillating perpendicular to the bond will have no effect. Therefore, covalently bound electrons are most likely to be excited by polarized light if the light is in the direction of the covalent bond. In single crystal samples, atoms are arranged in an ordered lattice. The orientation of a covalent bond in one unit cell is thus the same for that bond in every unit cell. Now the model for the excitation of a single covalently bound electron can be applied to the entire measured volume. Electrons from some constituents will thus be found to have a dependence on the polarization of the light source. This is technique is also applied to distinguish features in the valence band of $CuRh_{1-x}Mg_xO_2$ in Chapter VI.

Another PES technique used to amplify features in the VB, called resonant PES (RPES), has been utilized for this project. In RPES, the photon energy is tuned across the absorption edge of a specific core level. These photons excite both the VB electrons and the transition of the core level electrons to the unoccupied VB states. The resonant process of placing core level electrons into the VB of the same atom serves to increase the number of electrons excited from those VB states. When compared with off resonance PES spectra, RPES spectra can be used to locate

specific elemental compositions of the VB. The use of RPES to amplify rhodium in the VB is presented in Chapter VI.[18]

X-ray Emission Spectroscopy (XES)

When an electron is excited by photoemission, a hole is generated in the state that it previously occupied. An electron from the VB then drops down in energy to fill that hole. To account for the change in energy, a photon is created with an energy equal to the difference between the initial and final states. If the energy of the final state of the electron and the energy of the emitted photon are known, the initial energy of the electron can be calculated.

In the case of X-ray emission spectroscopy (XES), the photon energy is tuned to the absorption edge of a core electron in the sample. By tuning to the absorption edge, the emission of that single known core electron is maximized. Again, the core hole created by photoemission is filled by a higher energy electron from the VB. The emitted photons are measured as a function of their energies.

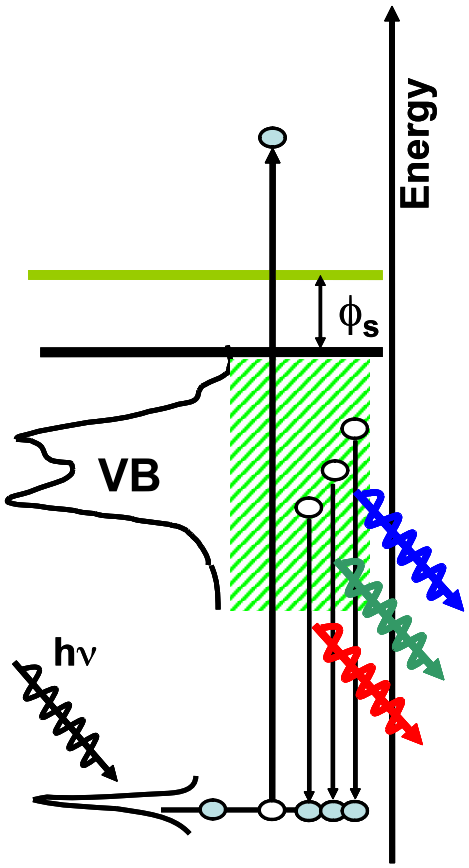

Figure 6. Diagram of XES in which a core level hole is filled by electrons from the VB with the emission of a photon equal to energy lost by the electron.[17]

The primary advantage of measuring VB spectra with XES is that it permits measurement of the VB with elemental sensitivity. When a core hole is filled, it may actually only be filled by electrons from

the same atom as the hole. So in the energy range of those transitions, the measured photons will generally correspond to electrons from the VB of only the selected atom (the atom to which the relevant core level belongs). This information can often be very helpful in the decomposition of a PES VB spectrum.

The shapes of XES spectra contain information about intensities and relative positions of splittings, but one cannot directly calculate binding energies. As an attempt, the energy of the final state in the emission process is taken to be the energy of the targeted core electron. With the emission spectrum, this data may of course be used to calculate the spectrum of the initial states of electrons involved in the process. This spectrum of initial states is actually only approximately equal to the equilibrium VB spectrum. The potential felt by the valence electron in the presence of a core hole is different from the equilibrium potential of the atom. The initial states of electron in this process should thus be more tightly bound to the nucleus. In analysis, calibration of XES spectra usually requires comparison with spectra of another technique like PES.

CHAPTER III

SAMPLES AND METHODS

Introduction

This chapter describes the experimental procedures used to prepare and measure these projects' samples. Some material contained within this chapter is briefly reiterated in the experimental sections of some of the following chapters so that they may stand alone as feasible papers. The intent of these sections is to provide additional details relevant to the projects.

Sample Preparation

Pulsed Laser Deposition (PLD) of Titanium Dioxide

PLD films are grown by focusing an intense laser pulse on the surface of a doped titanium dioxide (TiO_2) target. The target is sputtered in an oxygen atmosphere in order to compensate for the different sputtering yields between Ti and O. This serves the purpose of maintaining the stoichiometric 1:2 ratio between the Ti and O concentrations. The preparation of target materials with different concentrations of dopants almost guarantees the desired stoichiometric ratios in the films, as the different sputtering yields of the constituent elements are effectively compensated.[19]

TiO_2 Samples

The TiO_2 samples measured for this project have been grown at 350°C by PLD. They are Chromium (Cr)-only doped TiO_2, Nitrogen (N)-only doped TiO_2, and codoped TiO_2 nominally grown with equal parts of Cr and N.

The surfaces are prepared in air by wiping the surface first with acetone and then optical grade methanol. They are mounted on Molybdenum (Mo) sample holders and transferred via an ultra-high vacuum (UHV)-compatible load lock onto the sample manipulator in the UHV chamber. The pressure in the chamber is maintained at approximately 5×10^{-11} Torr. In the chamber the samples are degassed by heating them to approximately 150°C using a resistive heater on the manipulator. At this temperature, the pressure can rise as high as 2×10^{-10} Torr, but it equilibrates at approximately 5×10^{-11} Torr.

Measurement of the Cr-only doped sample indicated that it was "charging". This frequently occurs in oxides, as their bandgaps are often wide enough to insulate the charge flow from ground. The fundamental reason for charging is that holes are created by photoemission, the flow of electrons is not great enough to fill those holes, and the positively charged holes apply a retarding voltage to the measured electrons. This causes the photoemission spectra to be shifted to lower kinetic energies. One correction for this problem is to heat the semiconducting sample to increase its conductance. The Cr-only doped sample has thus been measured at an elevated 153°C. Since the N-only doped and codoped samples were not measured at elevated temperatures, it was necessary to confirm that measurement while heating does not affect the spectra. For this test, the codoped sample, which had not yet been removed from a holding carousel in vacuum, was heated to approximately 150°C and measured. There are no evident discrepancies in the heated versus room temperature spectra to indicate that the differing

conditions should nullify the comparison of the Cr-only doped sample measurements and other measurements.

$CuRh_{1-x}Mg_xO2$ Samples

The data presented in Chapter VI are measurements of single crystal Copper Rhodium Oxide ($CuRhO_2$) samples. The introduction of Magnesium (Mg) induces an insulator to metal transition in these samples, and they have been doped such that their stoichiometry is $CuRh_{0.9}Mg_{0.1}O_2$. Lattice constants are given for the dellafossite structure by the spacing between Rh atoms in the plane of the layers (*a*) and the spacing between RhO layers (*c*). In these samples $a = 3.074$ Å and $c = 17.095$ Å.[13]

Since the bonds between crystalline layers are weak enough, preparation of the surface of the sample been possible by cleaving in UHV. Cleaving is accomplished by gluing a ceramic post to the surface of the sample with silver paste. Once in vacuum the post is knocked off, and the top crystalline layer is removed with the paste. This exposes a new clean surface that has not been exposed to air.

Due to the requirement of a tunable photon source (see Chapter II covering Spectroscopy Techniques), photoemission measurements have been performed at the Advanced Light Source (ALS) synchrotron facility in Berkeley, CA. Emission measurements have been performed at the Elettra Laboratory synchrotron facility in Trieste, Italy.

Measurement

Electron Detector/Analyzers

Photoemission spectroscopy requires that the photoemitted electrons be measured as a function of their kinetic energies. The devices typically used for these measurements are electrostatic hemispherical analyzers. On a most fundamental level these analyzers count electrons with a kinetic energy within a small range, ΔE, of a given energy E_k. To understand the method of filtering electrons, the analyzer may be modeled as a spherical capacitor in which the outer hemisphere has a more negative potential than the inner hemisphere. The outward electric field forces negatively charged electrons in the hemisphere inward. For electrons with kinetic energy $E = \frac{1}{2} m_e v_e^2$ to pass through the analyzer along path R_0 (see Figure 7), the potential at R_0 should be $V_0 = \frac{E}{e}$.

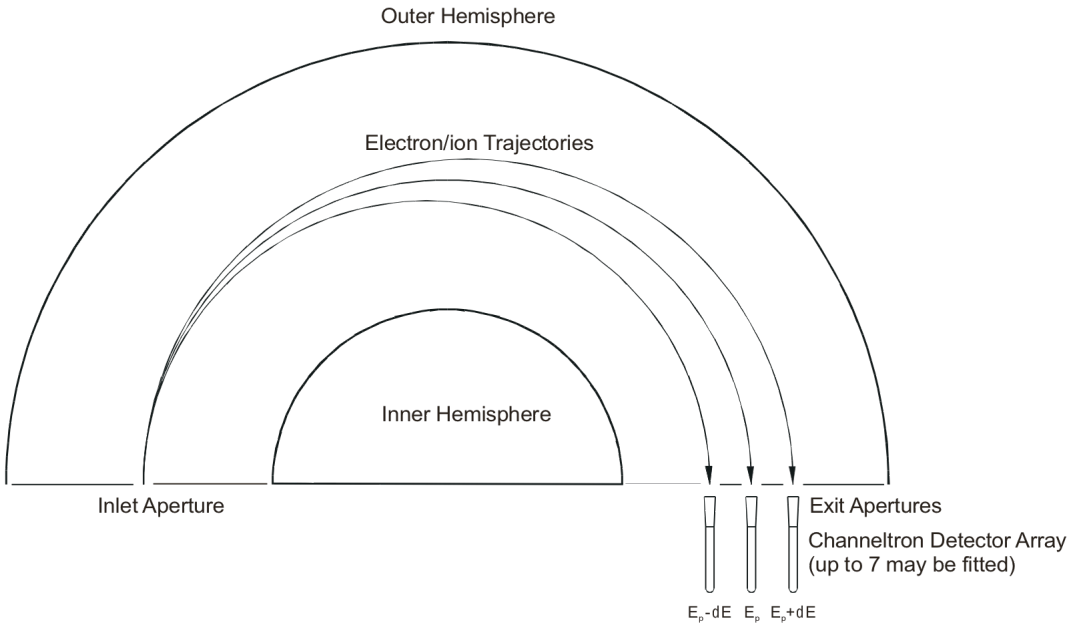

Figure 7. Diagram of electron trajectories where non-dispersed electrons with energy E_p follow the equipotential surface with radius R_0 between an inner hemisphere with radius R_1 and potential V_1 and outer hemisphere with radius R_2 and potential V_2.[20]

Since V_0 is defined as the potential at the equipotential surface, $V_0 = \frac{V_1 R_1 + V_2 R_2}{2R_0}$. R_0 is set as the average of R_1 and R_2 to center the equipotential surface between the inner and outer hemispheres. The applied potentials are thus $V_1 = V_0 \cdot \left(2\frac{R_0}{R_1} - 1\right)$ and $V_2 = V_0 \cdot \left(2\frac{R_0}{R_2} - 1\right)$. Using these formulas, an analyzer may vary the hemisphere potentials to scan over ranges of electron kinetic energies. Electron detectors then count the electrons that pass through the hemisphere.

The problem with this model is that the resolution changes with the kinetic energy of the measured electrons. Since ΔE increases linearly with the kinetic energy of the electrons passing through the analyzer hemisphere, V_1 and V_2 are held fixed so that only electrons with kinetic energy E_p, called the pass energy, pass through the hemisphere. Prior to entering the hemisphere, electrons with energy E_k are accelerated to the pass energy by a retarding potential. In this way, the analyzer electronics scan the energy range by varying the retarding potential, and resolution is maintained.

X-ray Photoemission Spectroscopy (XPS)

XPS measurements were performed using in-house equipment located at UT in the Science and Engineering Research Facility, Room 309. Specifically, the XPS chamber is equipped with an Al$K\alpha$ X-ray source (10-610E), monochromator (10-420), and an Omicron EA-125 multichannel electrostatic hemispherical analyzer. The angle between the X-ray source and the analyzer is 80°. Due to a limitation of the manipulator, the sample was measured at an angle of 39.7° with respect to normal emission (where at 0° the sample surface would be directly facing the analyzer).

To optimize measurement conditions such as resolution and count rate, there are several parameters available for the user to adjust. As described above, the pass energy may be decreased to increase resolution. However, increased resolution (decreased ΔE) leads to a lower count rate. Uncertainty in each measurement is proportional to the inverse square root of the number of counts, so comparable data at a lower count rate requires the user to increase the scan time.

Magnification mode affects the angle of accepted electrons, α. Scans at higher magnification thus have a lower resolution and a higher count rate. There are slits at the entrance and exit of the analyzer. Smaller slits serve the purpose of increasing the resolution of the analyzer by spatially filtering the spread of electrons in energy and momentum. However, smaller slits decrease the count rate.

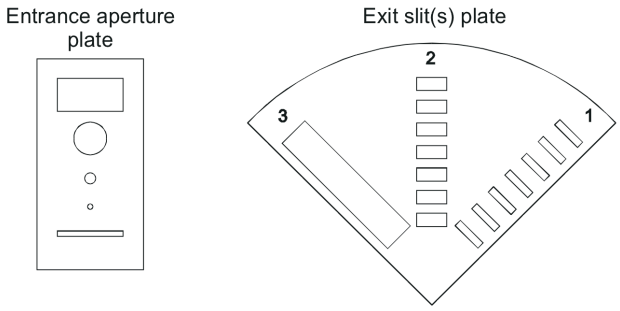

Figure 8. Detector entrance and exit plate layouts.[20]

Before running the experiment, spectra were measured using several combinations of the above parameters. The combination used for the measurement of TiO_2 was determined by optimizing the resolution while maintaining a reasonable count rate. For all XPS data presented, a pass energy of 25eV, high magnification mode, the 6mm entrance slit (bottom in Figure 8),and the 3mm exit slits (slit array 2 in Figure 8) have been used.

The resolution $\Delta E = E_p\left(\frac{d}{2R_0} + \alpha^2\right)$, where d is defined as the average of the two slit widths, R_0 for this analyzer is 125mm, and α is 0.14 radians. Therefore, the full width at half maximum resolution of the spectra due to the analyzer parameters is approximately 0.46eV.

Work Function Determination

In Chapter II, the kinetic energies (*KE*) of photoemitted electrons is related to their binding energies (*BE*) in the sample by $KE = h\nu - BE - \Phi_s$ where *hν* is the excitation photon energy and Φ_s is the spectrometer work function. For the measurement of TiO_2, Al Kα x-rays have been used to excite the electrons in the sample, so *hν* is known to be 1486.6eV. The work function, however, is analyzer dependent and occasionally variable. The best way to determine the work function is to use a very well defined feature in metals called the Fermi level, or chemical potential μ, defined as 0 on the binding energy scale. The Fermi level corresponds to energy of highest occupied electron states in a metal at 0K, though at higher temperatures the Fermi level is broadened by k_BT. To determine the work function of the Omicron EA-125 analyzer, the Fermi level of an aluminum foil was measured.

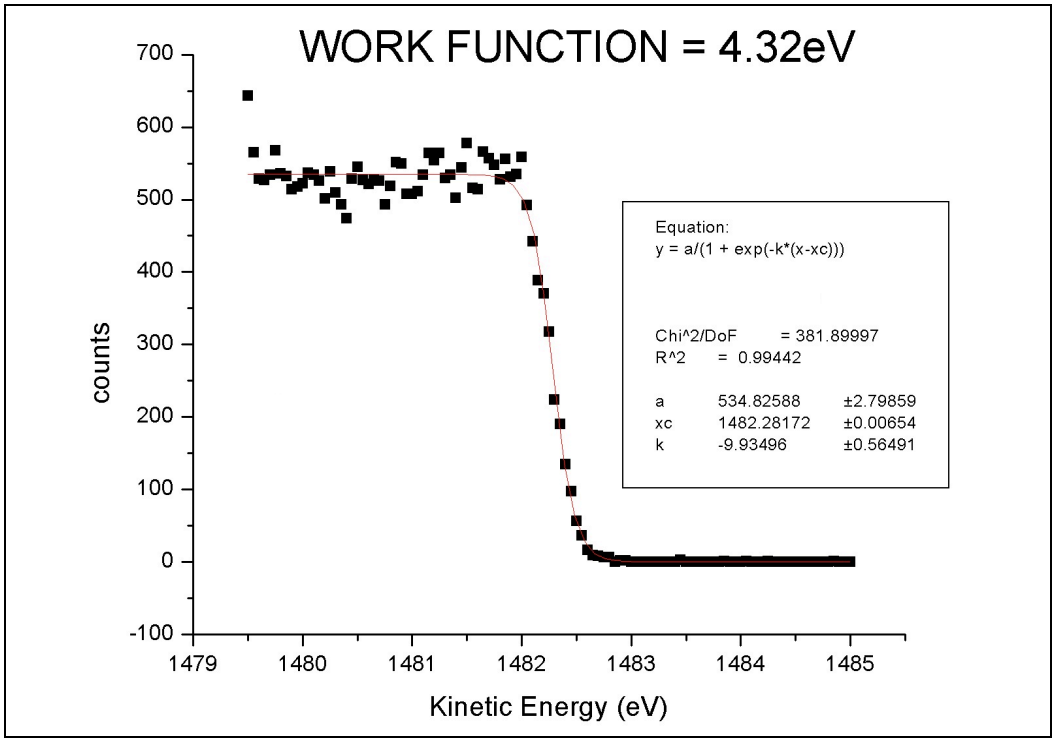

Figure 9. Fermi level of aluminum for determination of XPS analyzer work function.

After measuring the Fermi level of aluminum, the spectrum was fit with a scaled Fermi Dirac distribution function: $f(E) = \frac{1}{e^{(E-\mu)/(k_B T)} + 1}$. The point at which the amplitude is ½ the maximum amplitude of the Fermi function is μ. In Figure 9, electrons with kinetic energy *xc* correspond to this level. The work function is determined by setting the binding energy of the Fermi level to 0 and subtracting the value 1482.28eV from the photon energy 1486.6eV. This measurement accurately sets the work function at 4.32eV, a value within the reasonable range for the Omicron analyzer.

CHAPTER IV

QUANTITATIVE ANALYSIS

Introduction

My research has extensively employed photoemission (PES), a technique described in Chapter II, for its application to the study of condensed matter electronic structures and chemical compositions. While its description may be simplified to a brief few pages, nothing more than a qualitative identification of features could come from PES without a well-developed model for interpreting the magnitudes of the spectral intensities.

General Analysis

Background Subtraction

In PES, photoelectrons are detected as a function of their kinetic energies. A spectrum with intense peaks at discrete energies is formed because electrons from discrete energy levels in the sample are emitted with well-defined kinetic energies. However, the photoelectrons detected with these kinetic energies have not all been emitted from the corresponding energy levels in the sample. Due primarily to scattering processes, some photoelectrons lose kinetic energy as they exit the sample. Scattered photoelectrons that are still detected contribute to background. Since the photoelectrons that are important for analysis are those that come from the bound states in the measured samples, most analyses require that the background be subtracted. Unfortunately this is

not a trivial task, and no current method of PES background subtraction is entirely correct or even makes complete physical sense.

The simplest background subtraction technique assumes that the number of electrons scattered to a given kinetic energy is proportional the number of photoelectrons that have been measured as having greater kinetic energies. This makes some physical sense, but it is not correct. The problem with this background subtraction is that it assumes second and third scattering events have an equal probability of occurrence to the first. It thus creates a background in which electrons scattered from a single state have a greater propensity to be scattered to lower energies. When applied to wider ranges of spectra one finds that this background does not apply to ranges of kinetic energies over which intensity does not change since this background function continues to rise in these regions. The advantage of attempting this background subtraction is that it exposes the sharper rise in the background at the positions of peaks.

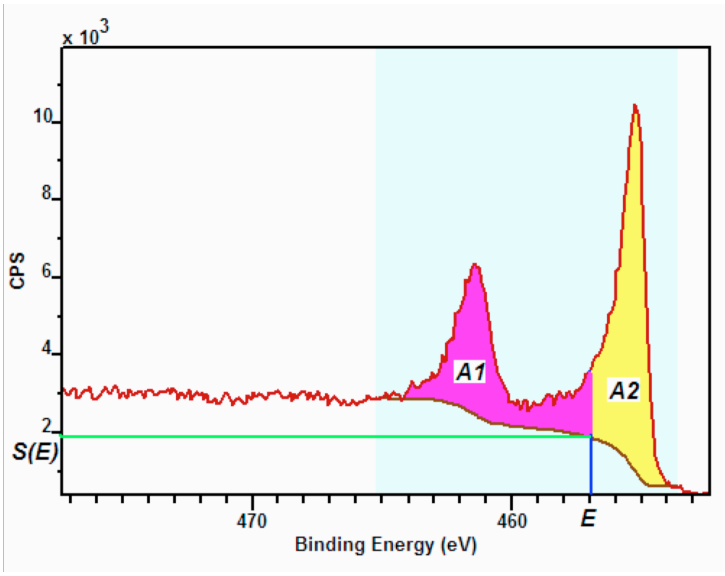

Figure 10. Ti2p spectrum with iterative Shirley background subtraction in which A2 is bound by the spectrum and most recent iteration's background and integrated from a highest kinetic energy (low binding energy) flat region to E.[21]

The first legitimate implementation of this sharp rise was in the form of the Shirley background. The Shirley background is only intended to apply to small ranges of the spectrum, and it assumes that the background is constant over all energy ranges in which there are no features. This is particularly applicable if one assumes that the majority of scattering events are first order processes. Given *A1* and *A2* in Figure 10, scanned energy *E*, and offset

intensity I_2, the Shirley background is given by:

$$S(E) = I_2 + \kappa \frac{A2(E)}{A1(E) + A2(E)} \qquad (2)$$

κ is defined as the step in the background due to the peaks and is usually equal to the difference in the intensities of the points that bound the total area.[21] Since the Shirley background is a function of peak areas that are background dependent, the implementation of this background is an iterative process.

Due to the assumptions made, the Shirley background is not exactly correct. This is exemplified by comparing the Shirley background of multiple peaks together versus individually. The first will generally estimate a larger background. For this reason it is believed that the sharp increase in the background due to the Shirley method is exaggerated. An alternative to the Shirley is the Tougaard background. Tougaard attempted to define the shape of the extrinsic energy loss tail that could be applied to the peaks in fitting.[22] Over the years there has been much debate about the meaning of those tails in the Tougaard background and the degree to which Shirley backgrounds should be applied.[24] The agreement is that background subtraction is complicated. For PES analysis in

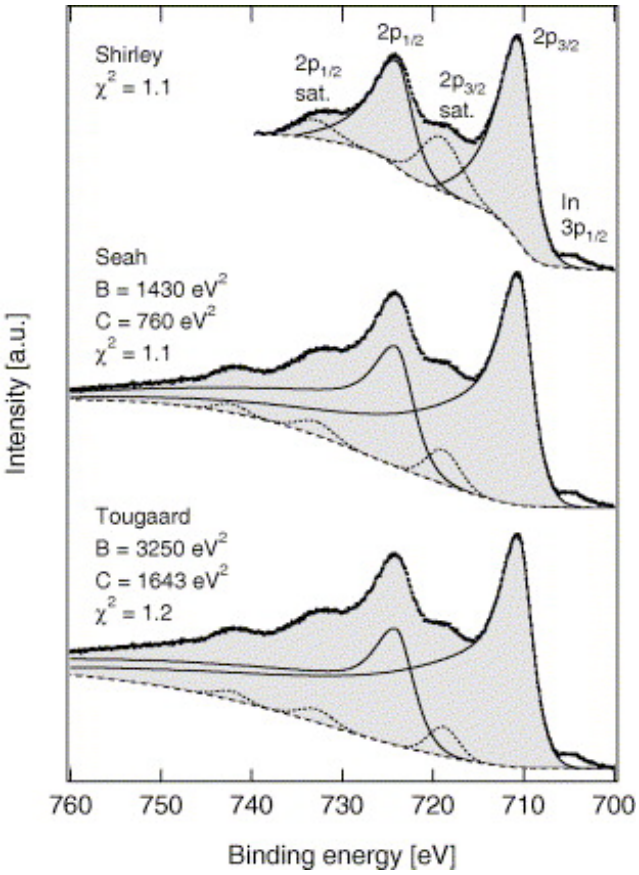

Figure 11. Application of several backgrounds to the same Fe2p PES spectrum.[23]

these projects, Shirley backgrounds have been applied with some discretion. For high kinetic energies, the Shirley applies very well. Some additional steps have been used to account for the backgrounds resulting from plasmons, but these are discussed in more detail in Chapter V as the steps are applied to TiO_2 spectra.

Peak Fitting

In PES and XES spectra, peaks frequently overlap. This can be due to the splitting of energy levels resulting from spin-orbit coupling, orbitals in different atoms with similar energies, or plasmons. The way to handle these overlaps in analysis is to fit each feature with peaks that make physical sense. With the correct lineshape to describe the features, the correct number of features, and some knowledge about the features, the spectrum may be decomposed into peaks each with a physical meaning.

First, the number of peaks that need to be applied must be determined. The number of states in the region may be ascertained from a binding energy table, a list of tabulated core levels and their energies. For the valence band one may assume that every constituent atom is represented.

The orbitals may then be further divided into split peaks by degeneracies due to spin-orbit coupling. Using the angular momentum quantum number l and spin angular momentum quantum number s, the possible total angular momentum quantum numbers are known:

$$j = |l + s|, |l + s - 1|, |l + s - 2|, \ldots |l - s| \qquad (3)$$

For a typical spectrum with multiplet splitting, $s = \frac{1}{2}$. The angular momentum quantum number is given by the orbital. For s-orbital states $l = 0$, for p-orbital states $l = 1$, and for d-orbital states $l = 2$. The degeneracy in angular momentum of each of these levels is equal to $2l + 1$. There is an

additional two-fold degeneracy due to the ½ spin of the electrons. Therefore, the number of electrons in an *s*-orbital is 2, in a *p*-orbital the number is 6, and a *d*-orbital the number is 10. Using Equation (3), $j = 1/2$ in *s*-orbital states. Since there is no degeneracy here, *s*-orbital states are expected to have just one peak in a spectrum. For *p*-orbital states $j = 3/2, 1/2$, so one may expect to see 2 peaks. Furthermore, due to the respective 4-fold and 2-fold degeneracies of the peaks' total angular momenta, one would expect the ratio of the peaks to be 2:1. In d-orbitals $j = 5/2, 3/2$, and the ratio of peaks is 3:2.[25]

The other notable features that are found in the spectra presented in Chapter V are plasmons. Plasmons result from the interaction of photoelectrons with conduction electrons. Due to the collective oscillation of the conduction electrons, the energy loss due to photoelectron interactions with plasmons is quantized and unique to the sample.[cite Moulder] After determining the plasmon frequency for a sample using a plasmon in one spectrum, one may predict plasmon peaks in all of the sample's spectra.

Having estimated the number of peaks, one must determine how each peak contributes to the entire spectrum. The energy level of the peak provides the average binding energy of the electrons bound in the corresponding state. Contributions to the intensity are quantified in the section below. This section will conclude with a physical description of the shape and width of each peak.

To derive the natural energy spread of a photoemitted electron, it makes sense to begin with Fermi's Golden Rule for the transition rate between two states *s* and *k* with perturbation $V(t) = V_o \cos(\omega t)$:

$$w = \frac{2\pi}{\hbar}\left|\langle k|V_0|s\rangle\right|^2 \rho_f\left(E_s + \hbar\omega\right) \tag{4}$$

Assuming a narrow final energy level, the density of states could be taken as a delta function, so $\rho_f\left(E_s + \hbar\omega\right) = \delta\left(E_k - E_s + \hbar\omega\right)$. However, after excitation to state *k*, there is a chance that an electron will decay back into state *s*. The probability of not decaying is $1 - w\,dt$, so $P_s(t + dt) = P_s(t)\left(1 - w\,dt\right)$. Given the characteristic $P_s\left(t_1 + t_2\right) = P_s\left(t_1\right)P_s\left(t_2\right)$ of the exponential function, one may derive the exponential decay law:

$$P_s(t) = e^{-wt} \tag{5}$$

Given the uncertainty in the lifetime of the hole state *s*, which equals the inverse of the decay rate, there is some uncertainty the state's energy. Heisenberg's uncertainty principle can thus be used to derive the width in energy of a distribution of states, Γ.

To derive a distribution of initial hole state *s*, the probability of a transition is integrated over a time that is much greater than the lifetime of the state:

$$P_{k\leftarrow s}(t = \infty) = \left|\langle k|\tilde{T}(t = \infty, 0)|s\rangle\right|^2 = \frac{\left|\langle k|V|s\rangle\right|^2}{\left(E_k - E_s - \Delta E_s\right)^2 + \frac{\Gamma^2}{4}} \tag{6}$$

Now, the probability of measured state having energy between *E* and *E* + *dE* is:

$$p(E)\,dE = \frac{1}{2\pi}\frac{\Gamma}{\left(E - E_s\right)^2 + \frac{\Gamma^2}{4}}\,dE \tag{7}$$

Hence the lineshape of a photoelectric peak has this form, called a Lorentzian function.[26] Having been derived from the exponential decay law and the uncertainty principle, it is no surprise that the Fourier transform of an exponential function is a Lorentzian function.[27]

Each peak is additional broadened by the inability to measure spectra with perfect resolution. Resolution effects are accounted for by convolving a Gaussian over the spectrum with a full width at half maximum value approximately equal to the resolution. This accounts for analyzer resolution, resolution of the monochromatic light source, and any thermal broadening of the features.

Quantitative Analysis of Photoemission

Generalize Differential Form

The first step in devising a model for quantitative analysis is to understand the actual data that has been measured. In the case of PES, the data contains measured intensities of photoelectrons as functions of their kinetic energies. Though often called counts, the truth is that these intensities have no inherent quantifiable meaning. In order to obtain quantified results it is necessary to relate intensities in a controlled manner. The quantitative comparison of data thus requires that all variables be either understood or not variable. In order to isolate those variables, a model has been developed, and this model has been used to make incredibly accurate assessments in experimental materials research.

To better understand the formulas presented below for predicting kinetic energy dependent electron detection, it is important to think about the excitation process, any energy losses, the paths of the photoemitted electrons, and the architecture of the analyzer. At the site of emission, the number of electrons that will be detected is affected by the number of electrons available to be photoemitted, the number of photons impinging on the volume capable of

exciting electrons, and the propensity that the photon will be absorbed. After the electron is excited it can go in any direction, so only those electrons excited in the direction of the nose of the analyzer will be detected. Electrons that are not on the surface of the sample also have a chance of being scattered by other atoms, and this can lead them to be either not detected or to have an artificially lower kinetic energy (contributes to the background at lower kinetic energies). Once in the detector window, electrons with different kinetic energies may then respond differently to the magnetic lenses and retardation potential. To address all these factors, the differential photoelectron peak intensity dN_k produced by subshell k and originating from volume $dxdydz$ at (x, y, z) has the form:

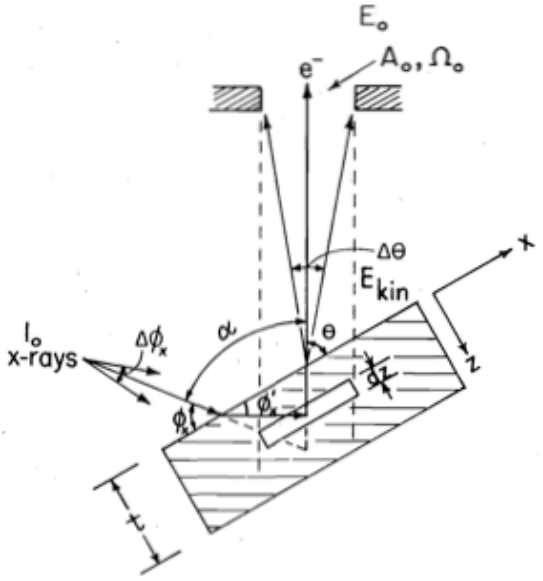

Figure 12: Sample and spectrometer geometry for calculation of photoelectron peak intensities.[28]

$$dN_k(\theta) = I_0\,\rho_k(x,y,z)\frac{d\sigma_k}{d\Omega}\Omega(E_{kin})D_o(E_{kin})e^{-z/\Lambda_e\sin\theta}dxdydz, \qquad (8)$$

$\frac{d\sigma_k}{d\Omega}$ = differential photoelectron cross section for peak k,
ρ_k = atomic volume density of peak k,
I_o = intensity of photon flux
Ω = acceptance angle,
D_o = instrumental detection efficiency,
t = thickness of layer,
θ = angle between sample normal and the nose of the analyzer = 39.7°,
Λ_e = inelastic mean free path

In this most general model the measured intensity of a photoelectron peak is linearly proportional to the photoelectron cross section (the photon energy dependent probability that the photoelectric

effect will occur) of the measured orbital, the atomic volume density, and the flux of the X-ray source. There are also several factors that depend on the kinetic energies of the photoelectrons.

Differential Photoelectron Cross Section

By the photoelectric effect, the absorption of light by an atom leads to the emission of an electron into a continuum of states. The differential photoelectron cross section is a function of the frequency of the incident radiation ω. For a plane wave excitation field with polarization $\hat{\mathbf{e}}$, momentum $\mathbf{p}$, and in the direction $\mathbf{n}$, $\exp\left(i\frac{\omega}{c}\hat{\mathbf{n}}\cdot\mathbf{r}\right)\mathbf{p}\cdot\hat{\mathbf{e}}$ is given as the perturbation of the transition from initial state s to final state k. In the dipole approximation it is assumed that the wavelength of electromagnetic wave used to excite the transition is much greater than the size of the atom, and $\exp\left(i\frac{\omega}{c}\hat{\mathbf{n}}\cdot\mathbf{r}\right)\approx 1+i\frac{\omega}{c}\hat{\mathbf{n}}\cdot\mathbf{r}+....$ Taking just the first term of the expansion, the matrix element representing the state transition may be simplified to $\langle k|\mathbf{p}\cdot\hat{\mathbf{e}}|s\rangle=\langle k|\mathbf{p}|s\rangle\cdot\hat{\mathbf{e}}$.[cite Merzbacher] The transition probability is given by:

$$P_{k\leftarrow s}=\frac{4\pi^2e^2}{\hbar^2m^2c\omega^2}\left|\langle k|\mathbf{p}|s\rangle\cdot\hat{\mathbf{e}}\right|^2N(\omega), \tag{9}$$

where $N(\omega)$ is the energy carried through a unit area per frequency integral. From the cross section (σ) definition, the energy absorbed in frequency interval $d\omega$ is $\sigma(\omega)N(\omega)d\omega$. The energy absorbed should be equal to the product of photon energy and the transition probability given in Equation (9). Therefore, for the number of electron eigenstates Δn in the frequency interval $\Delta\omega$, the differential cross section corresponding to a very sharply defined sold angle is:

$$d\sigma(\omega)=\frac{4\pi^2\alpha}{m^2\omega}\left|\langle k|\mathbf{p}|s\rangle\cdot\hat{\mathbf{e}}\right|^2\frac{\Delta n}{\Delta\omega}, \tag{10}$$

where $\alpha = e^2/\hbar c \approx 1/137$ is the fine structure constant. By defining initial states *s* as the various electron states in atoms using Hartree-Fock equations, total photoelectron cross sections may be calculated, and they have been tabulated in the Yeh and Lindau table of *Atomic Subshell Photoionization Cross Sections*.[29]

The differential cross sections with respect to the solid angle of acceptance are linearly proportional to the cross section, but also have a term that is dependent on the polarization of light, $\hat{\mathbf{e}}$. For linearly polarized light:[30]

$$\frac{d\sigma}{d\Omega}\left(h\nu, \hat{\mathbf{e}}\right) = \frac{\sigma_{n,l}}{4\pi}\left[1 + \beta_{n,l}P_2\left(\cos\gamma\right)\right] = \frac{\sigma_{n,l}}{4\pi}\left[1 + \frac{\beta_{n,l}}{2}\left(3\cos^2\gamma - 1\right)\right] \tag{11}$$

For unpolarized light:

$$\frac{d\sigma}{d\Omega}\left(h\nu, \hat{\mathbf{e}}\right) = \frac{\sigma_{n,l}}{4\pi}\left[1 + \frac{\beta_{n,l}}{2}\left(\frac{3}{2}\sin^2\alpha - 1\right)\right], \tag{12}$$

where for a given atom

$\hat{\mathbf{e}}$ = the polarization of incident radiation
$\sigma_{n,l}$ = the total cross section of the core level denoted with quantum numbers *n* and *l*
$\beta_{n,l}$ = the asymmetry parameter defined for the core level
α = the angle of the analyzer with respect to the x-ray source
γ = the angle between the polarization of the light and the outgoing photoelectron

For all s-orbitals, $\beta = 2$. Other orbital asymmetry parameters are tabulated in the Yeh and Lindau table of *Atomic Subshell Asymmetry Parameters* [29], though they have been tabulated more precisely by I. M. Band *et al* using relativistic Dirac-Slater potentials and further multipole expansion.[31]

Concentration Determination

The next step is to integrate over the measured volume (see Figure 12) to determine the total intensity. The first integration below assumes a semi-infinite homogeneous specimen with no overlayers. Since the mean free paths of electrons are much lower than the thicknesses of the presented samples, integration to infinity is reasonable. Homogeneity implies that ρ is treated as constant over the volume, and the lack of overlayers permits an integration from $z = 0$.

$$\begin{aligned} N_k(\theta) &= I_0 \rho_k \frac{d\sigma_k}{d\Omega} \Omega(E_{kin}) D_o(E_{kin}) \frac{A_o(E_{kin})}{\sin\theta} \int_0^\infty e^{-z/\Lambda_e \sin\theta} dz \\ &= I_0 \rho_k \frac{d\sigma_k}{d\Omega} \Omega(E_{kin}) D_o(E_{kin}) A_o(E_{kin}) \Lambda_e(E_{kin}) \end{aligned} \tag{13}$$

Since the measured intensity of peak k is proportional to the atomic volume density of the atom associated with peak k, chemical concentrations are related to the PES data. Concentration is determined by comparison of the atomic volume density of peak k to that of another sample constituent. By only caring about the comparison of the densities of peak k to peak l, one is additionally able to neglect any equivalent factors that contribute to both of their intensities. For a stable light source, the flux of photons is constant for all measurements performed on the same sample under identical conditions. For electron with similar kinetic energies (as is the case when analyzing a valence band which spans a range that is generally less than 10eV) the kinetic energy dependent factors cancel. To maintain generality, all factors except the photon flux will be left in the following calculations, but the transmission function will be defined as: $T(E_k) = \Omega(E_k) D_o(E_k) A_o(E_k)$. Now the concentration of constituent k with respect to l in a clean homogenous sample is:

$$\frac{\rho_k}{\rho_l} = \frac{N_k}{N_l} \frac{\frac{d\sigma_l}{d\Omega} T(E_l) \Lambda_e(E_l)}{\frac{d\sigma_k}{d\Omega} T(E_k) \Lambda_e(E_k)} \tag{14}$$

Overlayer Thickness Determination

If one of the constituents being measured is in an overlayer on the surface of the sample, as is the case for carbon (C), the electron attenuation term ($e^{-t\sin\theta/\Lambda_e}$) becomes very important. Furthermore, the entire volume cannot be considered homogenous, so integrations cannot span the entire sample. To compare the intensity of peak *l*, which corresponds to a constituent of the overlayer, and peak *k*, which corresponds to a constituent of the sample, one much integrate over each peak's respective volume. Therefore dN_l is integrated from $z = 0$ to $z = t$, and dN_k is integrated from $z = t$ to $z = \infty$. After integration, comparison of the intensities is written:

$$\frac{N_l}{N_k} = \frac{\rho' \frac{d\sigma_l}{d\Omega} T(E_l) \Lambda'_e(E_l)}{\rho \frac{d\sigma_k}{d\Omega} T(E_k) \Lambda_e(E_k)} \times \left[1 - e^{-\frac{t}{\Lambda'_e(E_l)\sin\theta}}\right] \times e^{\frac{t}{\Lambda'_e(E_k)\sin\theta}} \tag{15}$$

The goal of measuring an overlayer is generally not to measure concentrations, but rather the overlayer thickness *t*. To determine this thickness one must solve for *t* in Equation (15). Though the overlayer thickness estimations of the TiO_2 samples are not relevant to the conclusions of the research, the step is necessary to ensure other steps do not need to be taken in other parts of the analysis. In Equation (15) the unaddressed factors are the ratio of atomic densities (ρ'/ρ) and the attenuation length in the overlayer Λ'_e. Since doping concentrations are low, Ti atoms constitute approximately 1/3 of the total atoms in TiO_2. As a rough estimate the concentration of C in the overlayer is assumed to be approximately 0.5 (not unreasonable for the

case of carbon monoxide). By also assuming that the overlayer and specimen have similar densities, the concentration ratio is equal to the density ratio, and $\rho'/\rho \approx 3/2$.

For the ratio of attenuation lengths, it is acceptable to use the empirical proportionality of attenuation length to $E^{0.71}$ since the kinetic energies of photoelectrons corresponding to Ti2*p* and C1*s* orbitals are greater than 1keV.[32] However, in the exponentially decaying attenuation terms, the electron attenuation lengths are not part of a ratio, and thus their values must be established. One method for estimating these values is to use an empirical relation of electron energy and mean free path for metals. The formula given by Seah and Dench for metals is based on the universal curve depicted in Figure 13 and is written:[30]

$$\Lambda_e(E_k) = \left[\frac{1430}{E_k^2} + 0.54 \cdot \sqrt{E_k}\right] \overset{o}{A} \qquad (16)$$

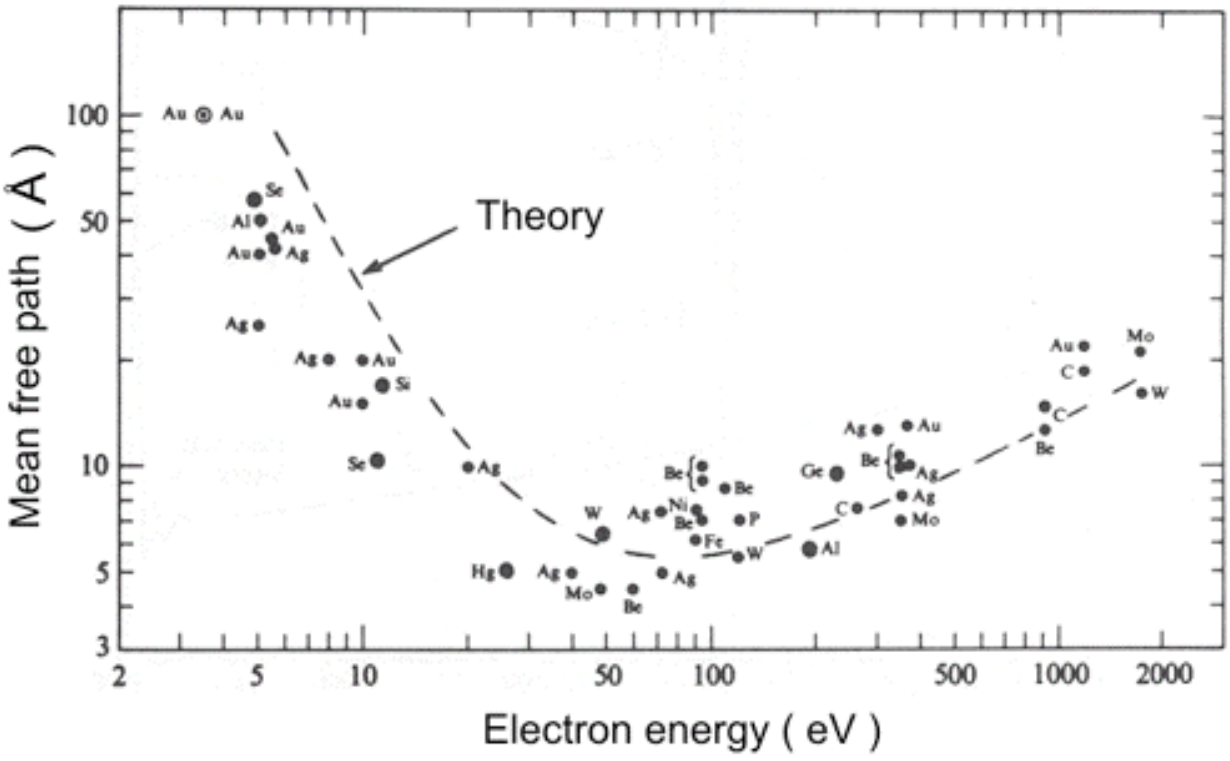

Figure 13: Universal curve for inelastic electron attenuation length of a function of electron energy.[33]

The overlayers are determined for each of the TiO_2 samples. Since the energies of electrons for C orbitals are relatively similar to those of Ti orbitals it is reasonable to estimate that $\Lambda_e'(E_{Ti}) \approx \Lambda_e'(E_C) \approx \Lambda_e(E_{Ti}) \approx \Lambda_e(1100eV) \approx 17.9\,\overset{o}{A}$. So now the thickness may be derived:

$$t = 17.9\,\overset{o}{A} \ln\left(\frac{M_C}{M_{Ti}}\frac{\rho}{\rho'} + 1\right)\sin\theta, \tag{17}$$

where $\frac{M_C}{M_{Ti}}$ = the ratio of C1*s* with respect to Ti2*p* for each sample found using Equation (14), and θ = 50.3°. For a more thorough discussion of the application of Equation (14) to the TiO_2 samples see the following Chapter V.

Table 1. Thickness of sample overlayer determined using measurement of C relative to Ti assuming a atomic density of 1/2 for C in the overlayer and 1/3 for Ti in the specimen.

SAMPLE	$\frac{M_C}{M_{Ti}}$	Thickness (Å)
350°C codoped:	1.097	7.56
350°C Cr-only doped:	1.183	8.01
350°C N-only doped:	0.551	4.31

Though these values are substantially less than the mean free path of the electrons, they indicate that these samples are not actually clean as was assumed in the analysis. Therefore the integral in Equation (13) should actually be taken from the base of the overlayer to infinity. Luckily the introduced term cancels out for electrons emitted from the assumed homogeneous sample.

Detailed Description of the Analysis of the Valence Band in $CuRhO_2$

Equation (13) describes the intensity of a photoelectron peak for a homogenous sample with no overlayer. Though most samples do not have a truly homogenous distribution of each constituent, a large enough mean free path permits integration over a large enough volume for homogeneity to be assumed. In the case of the rhodate (Rh) project, however, VB PES measurements have been made using excitation photons with energies between 60 and 200eV. Since the binding energies are VB electrons are very low, the kinetic energies of the photoelectrons are on the order of the photon energies. From Figure 13 one can see that the mean free path of electrons in this region is at a minimum. For a layered sample such a mean free path may make a tremendous difference. So rather than integrate over the volume, a layered sample would be better handled as a summation in which each constituent is assumed to exist in every other layer:

$$\begin{aligned} N_k(\theta) &= I_0 \frac{d\sigma_k}{d\Omega}\Omega(E_{kin})D_o(E_{kin})\frac{A_o(E_{kin})}{\sin\theta}\int_0^\infty \rho_k(z)e^{-z/\Lambda_e \sin\theta}dz \\ &= I_0 \frac{d\sigma_k}{d\Omega}\Omega(E_{kin})D_o(E_{kin})A_o(E_{kin})\Lambda_e(E_{kin})\sum_{i=0}^{\infty}\rho_k\left(\frac{2ai}{\sin\theta}\right)e^{\frac{-2ai}{\Lambda_e \sin\theta}}, \end{aligned} \tag{18}$$

where a is the lattice constant that defines the thickness of each layer. The above summation applies to the constituents whose first layer is the top layer. For constituents in the next layer, the counting must begin at a depth of $a/\sin\theta$. As before, matters are greatly simplified by comparison of intensities. The elements that are compared in the Rh analysis all have binding energies less than 10eV, and thus their photoelectrons all have energies approximately equal to hv. If Rh is assumed to be the top layer (though both are checked), the ratio of Rh to Cu is:

$$\frac{N_{Rh}}{N_{Cu}} = \frac{\rho_{Rh}\dfrac{d\sigma_{Rh}}{d\Omega}}{\rho_{Cu}\dfrac{d\sigma_{Cu}}{d\Omega}} \times \left[\frac{1 + e^{\frac{-2a}{\Lambda_e \sin\theta}} + \ldots}{e^{\frac{-a}{\Lambda_e \sin\theta}} + e^{\frac{-3a}{\Lambda_e \sin\theta}} + \ldots} \right] \approx \frac{\rho_{Rh}\dfrac{d\sigma_{Rh}}{d\Omega}}{\rho_{Cu}\dfrac{d\sigma_{Cu}}{d\Omega}} \times e^{\frac{a}{\Lambda_e \sin\theta}} \qquad (19)$$

Though just a constant scaling factor, for $CuRhO_2$ $\rho_{Rh} \approx \rho_{Cu}$ is approximately known. What remains in Equation (19) are the measured intensities, the photoemission cross sections, and a scaling factor that is dependent on the mean free paths of the photoelectrons. These are approximately calculated using the universal curve given by Equation (16).

The summation method is confirmed by Equation (13) in the limit where $\Lambda_e >> a$. In the region where $\Lambda_e < a$, as is the case in the Rh project, it becomes very necessary to apply the scaling factor to measurements of layered samples.

CHAPTER V

MEASUREMENT AND ANALYSIS OF DOPED TITANIUM DIOXIDE USING X-RAY PHOTOELECTRON SPECTROSCOPY

Introduction

The development of novel materials with tunable chemical reactivity and functionality as effective and low-cost photovoltaic and photocatalytic materials constitutes a vitally important area of condensed matter physics and materials chemistry. In this endeavor, proper introduction of a foreign species into a host material (i.e. substitutional doping) has been one of the most powerful approaches for tailoring the basic electronic band structure of an intrinsic semiconductor such as Si. Substitutional doping has been invoked to narrow the wide band gaps of metal oxide semiconductors, with titanium dioxide (TiO_2) as one premier material of choice for developing a wide variety of technological applications, ranging from photovoltaic devices to photocatalytic H_2O-splitting applications. There have been numerous attempts of doping TiO_2 using single-element doping and two-element codoping, but these have failed to produce a breakthrough. Most of the dopant atoms reside at undesirable interstitial sites, which not only compromise the effectiveness of band gap narrowing but also generate numerous electron-hole recombination centers. These doping schemes have proven to be ineffective, as the resulting doping levels fail to provide high-enough density of states in the band gap for photo-excitation at the desired wavelengths, limiting the photo-catalysis efficiency to well below the 10% target for commercial and industrial applications. The case of TiO_2 provides instances of a pressing state of affairs: a sound understanding of the microscopic mechanisms involved in doping oxide-

semiconductors is still lacking. Proper introduction of a foreign species into oxide materials is not a trivial matter: new doping schemes need to be developed and the microscopic mechanisms related to dopant incorporation need to be elucidated in order to control the basic electronic band structure of the host material.

A novel doping scheme, termed non-compensated n-p codoping, has recently been proposed as an enabling concept for narrowing the band gap of TiO_2. The concept embodies two key ingredients: the Coulomb attraction within the codopant pair enhances both the thermodynamic and kinetic solubilities, and the non-compensated nature ensures the creation of intermediate bands in the gap region of the host semiconductor, effectively narrowing its band gap. Its application may only be ensured by studying the following key issues: (a) dopant solubility; (b) band gap states; and (c) optical absorption and carrier mobility. Assuring solid solubility is the first step toward successful verification and exploitation of the codoping concept. Band gap reduction makes states available in the gap so that the carriers can be excited across the gap with energies belonging to the visible part of the solar spectrum. Band gap reduction is a necessary but not sufficient condition for an oxide semiconductor to be used for photovoltaic applications. The carriers must be free once they are introduced in the valence band (holes) or conduction band (electrons), otherwise no current can be generated, thus underlining the importance of carrier mobility.

X-ray Photemission Spectroscopy (XPS) has been used to focus on dopant solubility. The amount of dopants absorbed by various doping schemes have been compared by quantitative analysis of core level electrons. The data show that Cr/N non-compensated codoped samples are much more effective at incorporating substitutional Nitrogen than the single-doped samples.

Experimental

Samples

TiO_2 samples measured for this project have been grown at 350°C by Pulsed Laser Deposition (PLD). They are Chromium (Cr)-only doped TiO_2, Nitrogen (N)-only doped TiO_2, and codoped TiO_2 nominally grown with equal parts of Cr and N.

The surfaces are prepared in air by wiping the surface first with acetone and then optical grade methanol. They are mounted on Molybdenum (Mo) sample holders and transferred via an ultra-high vacuum (UHV)-compatible load lock onto the sample manipulator in the UHV chamber. The pressure in the chamber is maintained at approximately 2×10^{-11} Torr, except during sample heating. In the chamber the samples are degassed by heating them to approximately 150°C using a resistive heater on the manipulator. At this temperature the pressure can rise as high as 2×10^{-10} Torr, but it equilibrates at approximately 5×10^{-11} Torr.

Procedure

XPS measurements have been performed using a UHV chamber equipped with an Al$K\alpha$ X-ray source (10-610E), monochromator (10-420), and an Omicron EA-125 multichannel electrostatic hemispherical analyzer. The angle between the X-ray source and the analyzer is 80°, and the sample was measured at an angle of 39.7° with respect to normal emission to the analyzer.

A pass energy of 25eV has been used for all measurements. With consideration given to the analyzer pass energy, slits, magnification, and radius, the FWHM resolution (ΔE) of the analyzer is calculated to be approximately 0.46eV.

At room temperature Cr-doped samples were charging (see Chapter III section on TiO_2 samples). To correct this issue, measurements of Cr-doped sample were performed at an elevated temperature of 155°C. Comparison of room temperature and elevated temperature scans of the non-charging codoped sample indicates that such heating does not impair the data.

For each sample, core level electrons bound by Ti, O, Cr, N, and carbon (C) nuclei were measured as functions of their energies. Counts were increased over regions with low signal to noise ratios by increasing the number of analyzer sweeps over the regions.

Results and Discussion

The work function, Φ_s, of the analyzer was determined by measurement of the Fermi level of Aluminum, and found to be 4.32eV. Using the analyzer work function and that the energy of the impinging photons ($h\nu$) is 1486.6eV, the electron data as a function of kinetic energy (KE) is converted to binding energy (BE) using: $BE = h\nu - KE - \Phi_s$.

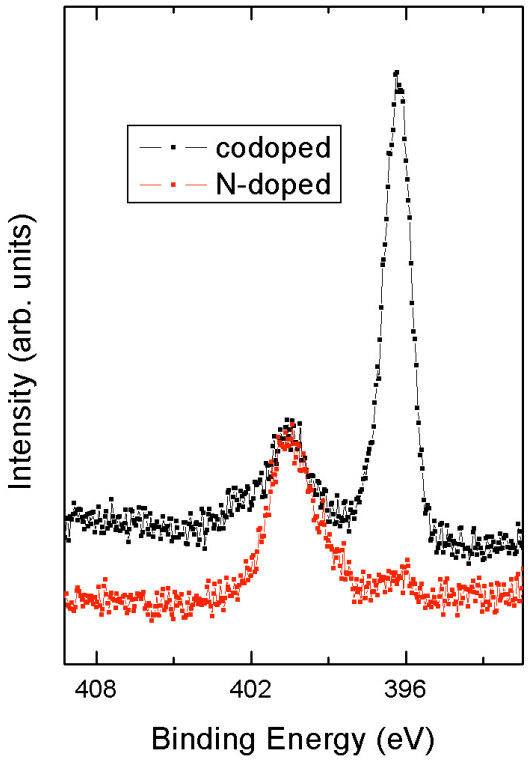

Figure 14. N1s core level spectra of N-only doped and Cr/N codoped TiO_2 grown at 350°C indicate that the non-compensated codoped sample is much more effective in incorporating substitutional N (lower binding energy feature) than the single doped sample.

The first qualitatively evident conclusion to be drawn from the data is that N is more effectively incorporated in the codoped sample. In Figure 14 the N1*s* spectra measured in the N-only and codoped samples are compared. The peak at 400eV

corresponds to surface and interstitial N. The peak that is shifted toward lower binding energy by 4eV is substitutional N, the N that is bound to Ti. In the Figure 14 spectrum it is evident that the codoped sample is more effective at incorporating substitutional N. Whether or not the sample doping is non-compensated cannot be determined without a quantitative analysis of the data.

In Chapter IV, the method for quantitatively determining the concentrations of sample constituents is detailed. From the most fundamental Equation (8) of the differential photoelectron peak intensity, equation (14) has been derived which relates the concentrations of constituents corresponding to peaks *k* and *l*. The factors that need to be known in order to find these ratios are the differential photoemission cross sections of each orbital, the kinetic energy dependent factors $T(E)$ and $\Lambda_e(E)$, and the measured peak intensities corresponding to each orbital.

Since the angle of the x-ray source with respect to the analyzer is 80°, the asymmetry parameter has been taken into account for calculation of the differential photoemission cross section. The total cross sections ($\frac{\sigma_{n,l}}{4\pi}$) and the asymmetry parameters for non-*s*-states (β) have been calculated by Yeh and Lindau. Since the XPS x-ray source is not polarized, the differential cross sections have been calculated using Equation (12). The results are tabulated below:

Table 2. Differential cross section calculated using tabulated cross section values and asymmetry parameters given an angle between x-ray source and analyzer of 80°.[29]

Orbital	**Cross section:** $\frac{\sigma_{n,l}}{4\pi}$	**Asymmetry:** β	**Differential CS:** $\frac{d\sigma_{n,l}}{d\Omega}$
Ti2p	0.1069	1.370	0.140
Ti2s	0.0440	2.000	0.0640
Cr2p	0.1577	1.435	0.209
N1s	0.0240	2.000	0.0349
O1s	0.0400	2.000	0.0582
C1s	0.0130	2.000	0.0189

Though the kinetic energy dependent factors are generally the most difficult to understand, some of these factors are empirically known. The first of these, $T(E)$, is the XPS analyzer's transmission function (proportional to $E^{-0.99}$ in the case of the Omicron analyzer [20]). The other is the inelastic attenuation length (approximately proportional to $E^{0.71}$ for core levels [32]).

Each concentration in the doped TiO_2 samples has been determined by comparison with the 2*p* and 2*s* Ti orbitals. The final formula used to calculate each concentration is (in the case of comparison with Ti2*p*):

$$\frac{\rho_k}{\rho_{Ti2p}} = \frac{N_k}{N_{Ti2p}} \frac{\frac{d\sigma_{Ti2p}}{d\Omega}}{\frac{d\sigma_k}{d\Omega}} \left(\frac{E_{Ti2p}^{-0.28}}{E_k^{-0.28}} \right) \tag{15}$$

Data analysis begins with the determination of photoelectron peak intensities (proportional to *N*). To normalize the flux, each spectrum is divided by the number of times the analyzer scanned the spectrum's energy range to generate the spectrum (called the number of sweeps). Since the dwell time for each data point was held at a fixed 0.2 seconds for the duration of the experiment, division by the sweep numbers normalizes all data to the same arbitrary intensity units.

At some point during analysis the kinetic energy dependent factors must be applied. It is best to directly apply these to all the spectra plotted in kinetic energy (point by point) by dividing the spectra by $E^{-0.28}$. However, since the energy dependence is very low, it is acceptable to assume a constant factor over a short-range spectrum. If this assumption is made, these factors may be applied to the integrated peak intensities after completion of the next few steps.

Now the number of measured photoelectrons associated with a feature is proportional to an integration of the photoelectron peak associated with that feature. To isolate the features, Shirley backgrounds are first subtracted from each spectrum in the manner described in Chapter IV. In the cases of isolated core levels like the N1*s* and O1*s* states, the background subtraction is adequate for removing all irrelevant features from the spectra. N_k is found by the numerical integration of the peak k that remains after background subtraction.

In spectra containing overlapping peaks, some additional work is generally required to isolate the peaks for integration. For instance, the binding energy of the Ti2*s* orbital is 560.9eV, and the binding energies of the split Cr2*p* orbital states are 583.8eV and 574.1eV. In addition, quantized electron gas oscillations, called plasmons, capture discrete quantities of the emitted electrons' energies. This leads to the presence of Ti2*s* plasmon features at approximately 574eV and 587eV on the binding energy spectrum. In cases such as this it helps to have measured a parent sample for comparison of spectra. No pure TiO_2 sample has been measured, but this energy range in the N-only doped sample only exhibits Ti. To determine the Cr2*p* in the codoped and Cr-only doped samples, the N-only doped sample's Ti2*s* spectrum is subtracted from those sample as depicted in Figure 15. To account for differences in measurement conditions, the Ti2*s* spectrum of the N-only doped sample is scaled by multiplication and then offset to match the Ti2*s*/Cr2*p* spectra of the codoped and Cr-only doped samples. After subtraction, the background of the remaining Cr spectrum is approximated with a polynomial, and a numerical integration is applied over the Cr peaks.

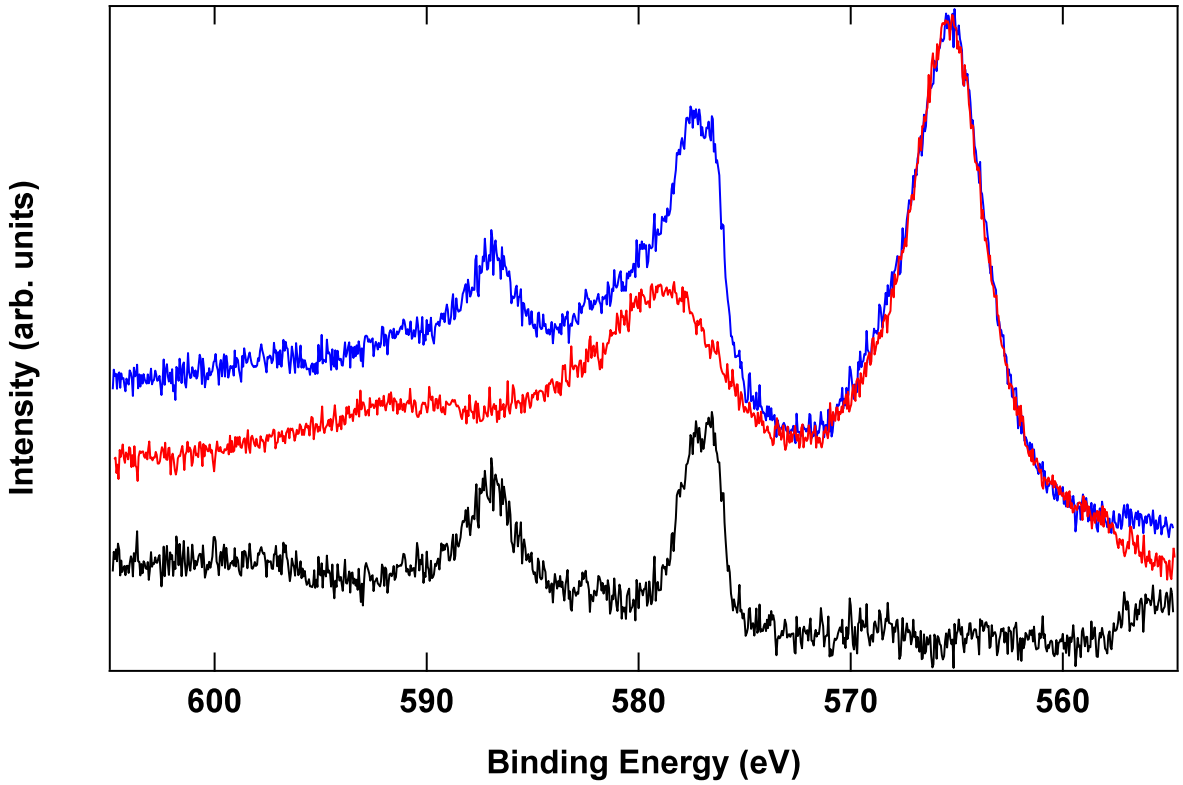

Figure 15. Cr-doped TiO_2 spectrum of Ti2*s* and Cr2*p* orbitals in blue, N-doped TiO_2 spectrum of Ti2*s* in red, and the difference between the two which represents Cr2*p* in black. Cr2*p* intensity determined after subtraction of polynomial background.

To determine Ti2*s* in the N-only doped sample, the Shirley background is removed and the remaining peaks' areas integrated. To determine the Ti2s in the other samples, the scaling factors used to match spectra in the previous determination of Cr are applied to the determined intensity of Ti2s in the N-only doped sample. Having obtained all necessary peak intensities, differential photoemission cross-sections, and electron energies, concentrations have been determined by equation (15) and tabulated in Table 3.

Table 3. Concentrations of constituents relative to Ti in samples determined by XPS quantitative analysis. C1s values are shaded because carbon is in overlayer and not a sample constituent.

SAMPLE	Element (Orbital)	Ratio wrt Ti (2*p*)
350°C codoped:	Cr (2*p*)	0.0508
	N (1*s*) substitutional	0.0255
	N (1*s*)	0.0382
	O (1*s*)	1.996
350°C Cr-doped:	Cr (2*p*)	0.0658
	N (1*s*) substitutional	0
	N (1*s*)	0.0131
	O (1*s*)	2.005
350°C N-doped:	Cr (2*p*)	0
	N (1*s*) substitutional	0.00194
	N (1*s*)	0.0154
	O (1*s*)	1.996

The qualitative conclusion that N substitution is enhanced by codoping TiO_2 with Cr is confirmed quantitatively. Though the total amount of N on and in the sample is low, the N that has been absorbed into the crystal constitutes 67% of the total N. Given that the Cr/N ratio is 1.99 and not 1, the nominal non-compensated doping scheme does not seem to be the true doping scheme.

CHAPTER VI

ELECTRONIC STRUCTURE DETERMINATION OF THERMOELECTRIC RHODIUM BASED OXIDES USING SOFT X-RAY SPECTROSCOPIES

Introduction

Thermoelectric materials are classified by their high efficiency in the conversion processes of heat to electricity. With the ability to generate energy from any thermal gradient, the synthesis of new thermoelectric materials is a crucial part of the general effort to conserve our sources of energy. A thermoelectric device has the capability of capturing geothermal energy, the heat loss inherent to all engines and generators, and as improvements are made, these devices may also be applied to solar thermal energy generation.

Oxide thermoelectrics in particular are appealing because they are stable at high temperatures and in air. For years the standard oxide theromoelectrics have been cobalt compounds such as Na_xCoO_2.[34] Recently, magnesium-doped rhodium oxides with formula unit $CuRhO_2$ and delafossite-type structure have been found to exhibit an exceptionally high figure of merit (a dimensionless parameter used to rate a material's performance) at high temperatures.[13] Since rhodium (Rh) and cobalt (Co) have the same number of electrons in their outer shells, a compelling question to ask is whether the occurrence of thermoelectricity in oxides is directly connected to the presence of six electrons in the outermost d orbital of the Co and Rh atoms. It has been proposed that thermoelectricity in the cobalt oxides is closely tied to the degrees of freedom of the states of the d^6 ion (Co) and the presence of these electronic states at the Fermi level (E_F), the ones responsible for transport of charge.[10] Experimental evidence for the presence

of Rh-derived states at E_F in thermoelectric Rh oxides would confirm the significance of, specifically, the d^6 ion.

The goal of this research has been to experimentally study the electronic structure of Mg-doped $CuRhO_2$ thermoelectric materials with various soft X-ray spectroscopies located in state-of-the-art synchrotron radiation facilities such as the Advanced Light Source (ALS) in Berkeley, CA. These techniques, which include photoemission (PES), resonant photoemission (RESPES), and X-ray emission (XES), are extremely valuable for determining the electronic structure of materials with elemental sensitivity, including the nature of the states at the E_F.

These results will assist in obtaining a correct description of the microscopic mechanisms responsible for the high efficiency of oxide thermoelectrics, thus facilitating the future design of more ideal thermoelectrics.

Experimental

Samples

Single crystal copper rhodium oxide ($CuRhO_2$) samples have been prepared by collaborator Takao Sasagawa. The introduction of Magnesium (Mg) induces an insulator to metal transition in these samples, and they have been doped such that their stoichiometry is $CuRh_{0.9}Mg_{0.1}O_2$. The crystals have a copper (Cu) based dellafossite-type structure with layers of hexagonal RhO building blocks that are isomorphic to the CoO building blocks in the sodium cobaltate thermoelectrics.[34] Spacing between Rh atoms in the plane of the layers, *a*, is 3.0741(1) Å. Spacing between RhO layers, *c*, is 17.0952(3) Å.[13]

Since the bonds between crystalline layers are weak enough, the surface of each measured sample was cleaved in UHV prior to measurement. All measurements were made at room temperature at UHV pressures.

Procedure

Due to the requirement of a tunable photon source for some of these specific techniques (see Chapter II covering Spectroscopy Techniques), photoemission measurements have been performed at the Advanced Light Source (ALS) synchrotron facility in Berkeley, CA. Emission measurements have been performed at the Elettra Laboratory synchrotron facility in Trieste, Italy.

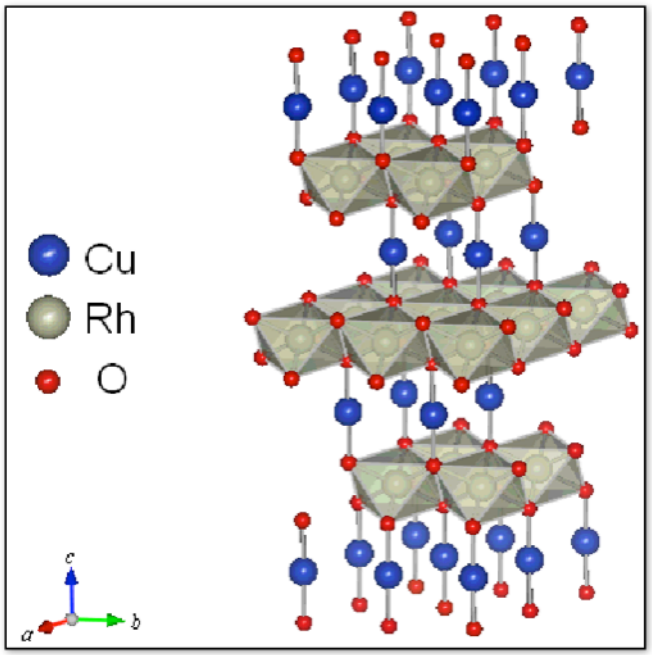

Figure 16. Diagram of the CuRhO2 with a dellafossite-type structure.[35]

Several techniques have been used to experimentally verify the presence of Rh at E_F. Polarized light has been used to exploit a dichroic effect of some crystals. In single crystal samples, the orientation of a covalent bond in one unit cell is the same for that bond in every unit cell. If the light source is polarized along the bond it will have a greater chance of exciting those electrons. Electrons from some constituents will thus be found to have a dependence on the polarization of the light source.

Resonant PES (RPES) has been utilized to amplify features in the VB. In RPES, the photon energy (*hv*) is tuned across the absorption edge of a specific core level. These photons

excite both the VB electrons and the transition of the core level electrons to the unoccupied VB states. The resonant process of placing core level electrons into the VB of the same atom serves to increase the number of electrons excited from those VB states. When compared with off resonance PES spectra, RPES spectra can be used to locate specific elemental compositions of the VB.[18]

The dependence of the PES peak intensities on their cross sections, calculated quantities that represent the propensity of a photon to photoemit an electron, has additionally been used to confirm the presence of Rh at E_F. The fundamental idea of this technique is that the measured intensity of a peak corresponding to an electron orbital should be proportional to the PES cross section of the orbital. Since cross sections are dependent on the photon energy used to excite them, constituent features should follow the trends of their cross sections. The Rh *4d* orbital has a cross section minimum, called the Cooper minimum, at $h\nu \approx$ 105eV. If Rh is at the Fermi level, one would expect a spectral decrease in the intensity of the Fermi level in a spectrum excited by photons in the 105eV range.

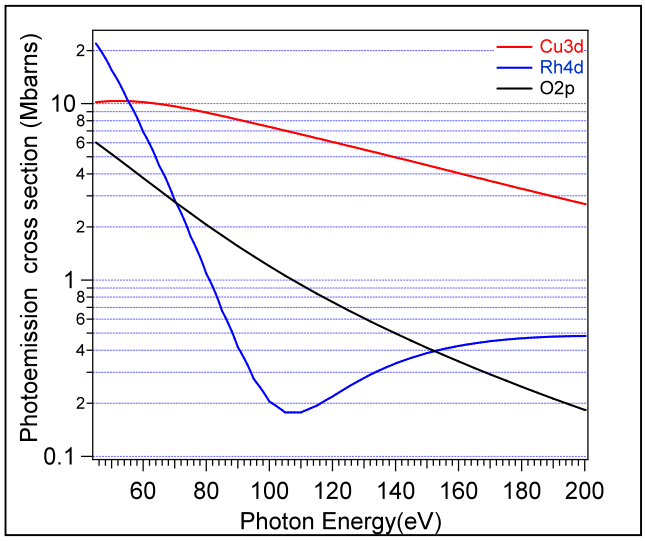

Figure 17. Photon energy dependent PES cross section calculations of $CuRhO_2$ VB constituents in the region of the Rh Cooper minimum.[29]

Though not for the direct confirmation of the hypothesis, x-ray emission (XES) has been used for decomposition of photoemission spectra. In XES a core hole electron is excited by photoemission and then filled by an electron from the VB. The measurement is a spectrum of the light emitted as the transitioning electrons lose energy to fill the core level hole. XES is valuable

for VB decomposition as it allows for measurement of the VB with elemental sensitivity. The technique is implemented in this chapter, and a more extensive description is provided in Chapter II.

Results and Discussion

The data have unanimously concluded that the states at the Fermi level are Rh-derived. Out-of-plane polarized light excited states at the Fermi level, displayed in Figure 17, indicating the presence of a covalently bound electron lying along the c-axis in the crystal. These two states resemble the Rh states that are predicted by local density approximation calculations.[13] However, this data is of course not adequate to make the full claim that these states are Rh-derived.

To measure the RPES valence band (VB) spectrum in Figure 18, an absorption edge of Rh has been excited by photons with $h\nu$ = 497.08. The RPES spectra excited by out-of-plane polarized light show a spectral

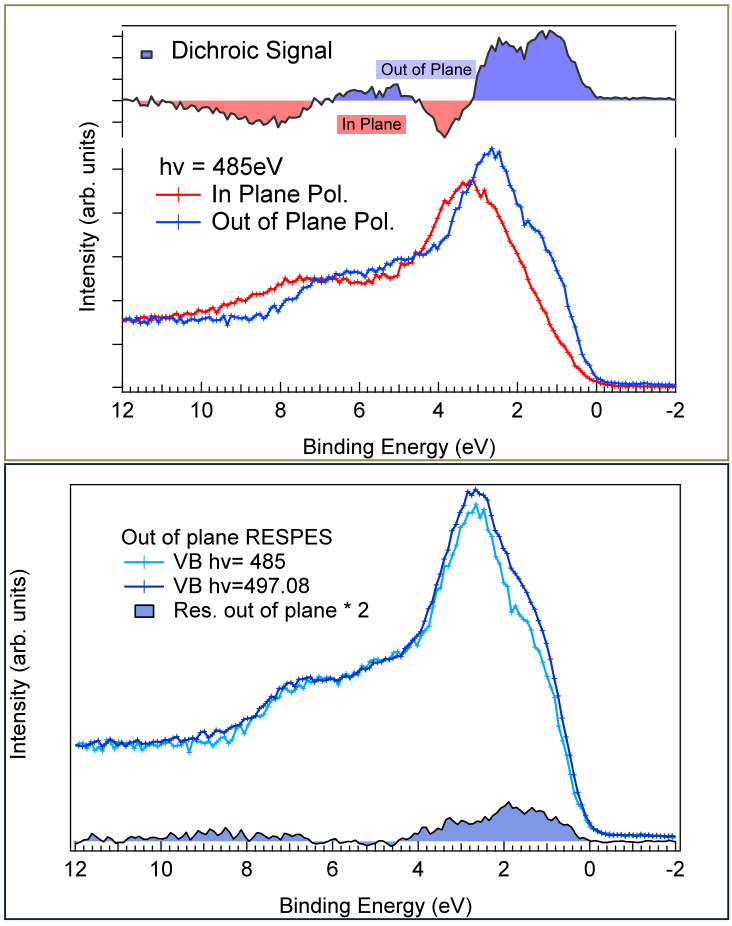

Figure 18. Top: Excitation light polarization dependent photoemission spectra indicating that electron states at the E_F lie along the c axis. Bottom: Resonance of Rh in the valence band at the E_F by out-of-plane polarized light.

increase at the Fermi Level for the spectrum that was measured on-resonance. Due to the low cross section of the excitation for in-plane polarized light, no resonance was evident in the spectrum excited by an in-plane electric field. The RPES spectra thus serve the purpose of indicating that the two states at the Fermi level are Rh-derived and that the polarization dependence of the Fermi level makes sense for the measurement of the Rh *4d* states.

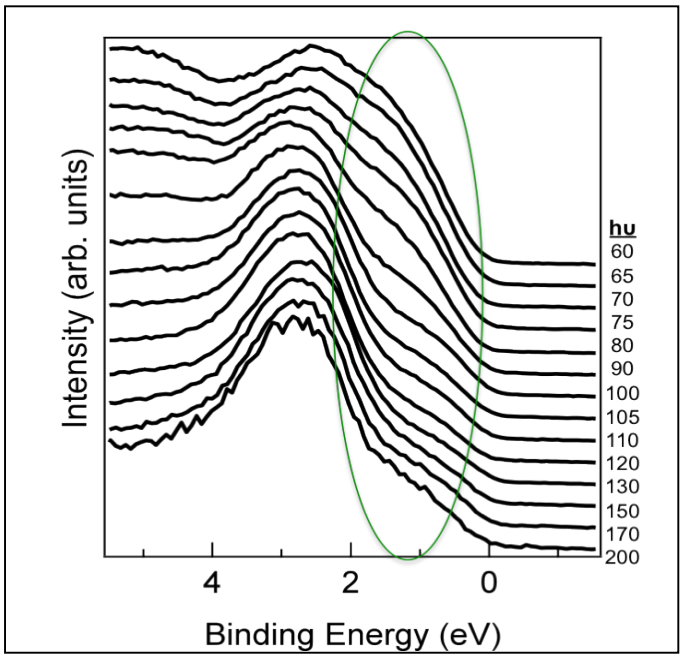

Figure 19. *hv* dependent measurements of the VB using PES. Spectra cropped to magnify the states at E_F.

Though RPES data is fairly conclusive, spectra of the Fermi level excited by photon energies in proximity to the Cooper minimum of the PES cross section should follow the trend of the Rh *4d* cross section. Though the cross section is low, the *hv* dependent spectra have been measured using in-plane polarized light. The idea is that even though the relative excitation of Rh with respect to Cu and O may be lower, the trend of Rh intensities as a function of *hv* should be unaffected. The data in Figure 19 immediately support the hypothesis. The spectral weight of the Fermi level excited by 60eV photons is qualitatively much greater that the weight of the Fermi level excited by 105eV photons, which is in very good agreement with the cross section calculation in Figure 17.

A quantitative confirmation of the hypothesis is necessary to definitively determine the Fermi level. It is first necessary to decompose the VB spectra. To do so requires some

knowledge of the states in the VB, and since the VB electron states are material dependent, this information must be acquired experimentally.

XES has been used to elucidate some information about the specific states in the VB. In Figure 20 the VB of oxygen (O) is determined by measuring the emission spectrum of the *2p* to *1s* transition of O. The information that may be gleaned from such an XES spectrum is the number of degenerate states and their energy splitting. The information that is not conserved in the transition between these techniques includes the absolute binding energies of the measured states, the Lorentzian widths of the peaks due to the differences in the transitions, and even the relative amplitudes due to differences in the transition probabilities between states. However, even the non-conserved information should not be entirely disregarded. The measurements still of course reflect many elements that are inherent to electron states, so vastly different results between techniques should be regarded as unexpected and worthy of further consideration.

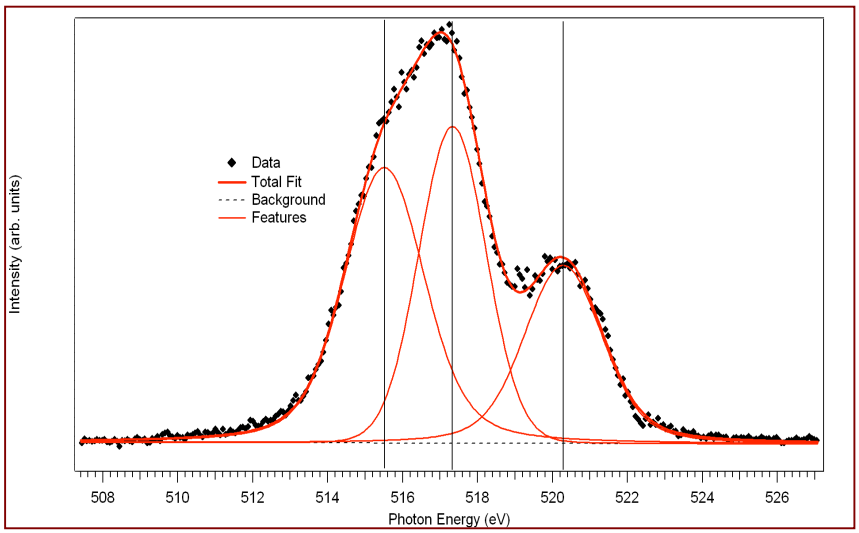

Figure 20. XES measurement of photons emitted from O *2p-1s* transition revealing the VB with elemental sensitivity. *hv* = 545eV and photon energies are those of emitted photons.

With information about the O and Cu states in the VB from their respective XES measurements (The Rh core level cross sections were too low to measure the Rh *4d* states with XES), the *hv* dependent PES spectra may be decomposed. First, Shirley backgrounds are subtracted from all spectra. Voigt peaks, which define a Lorentzian distribution of states over

which a Gaussian is convolved to account for the measurement resolution, are applied for each peak determined from the XES measurements. The difference in energy of each given peak within an orbital is constrained by the XES measurements. Features are also placed on the spectrum in expected locations. For instance, the main Cu feature is initialized to the position of the largest point in the PES spectra. After placement of known peaks, other necessary peaks are placed to fill the gaps, and namely 2 peaks of unknown origin are placed near the Fermi level. Initially just 1 peak was placed, but time made it apparent that 1 peak could not suffice.

The objective while fitting data is to make as few assumptions as possible, constrain as many elements as can be legitimized, and to make physical sense of all operations applied during the fitting process. In the case of this project, 13 similar spectra of the same material were available for analysis, so the maintenance of continuity of the parameters over the spectra has functioned as the verification process of the fitting procedure. The parameters that do not vary with photon energy are the binding energies of all states, the resolution of the measurements, and the transition rates of electrons decaying into VB states. Since the cross sections vary with photon energy, as is the dependence this section is attempting to exploit, the amplitudes are not held fixed between spectra. Relative amplitudes of features belonging to the same orbital are, however, mostly maintained. One of the resulting fits is depicted in Figure 21.

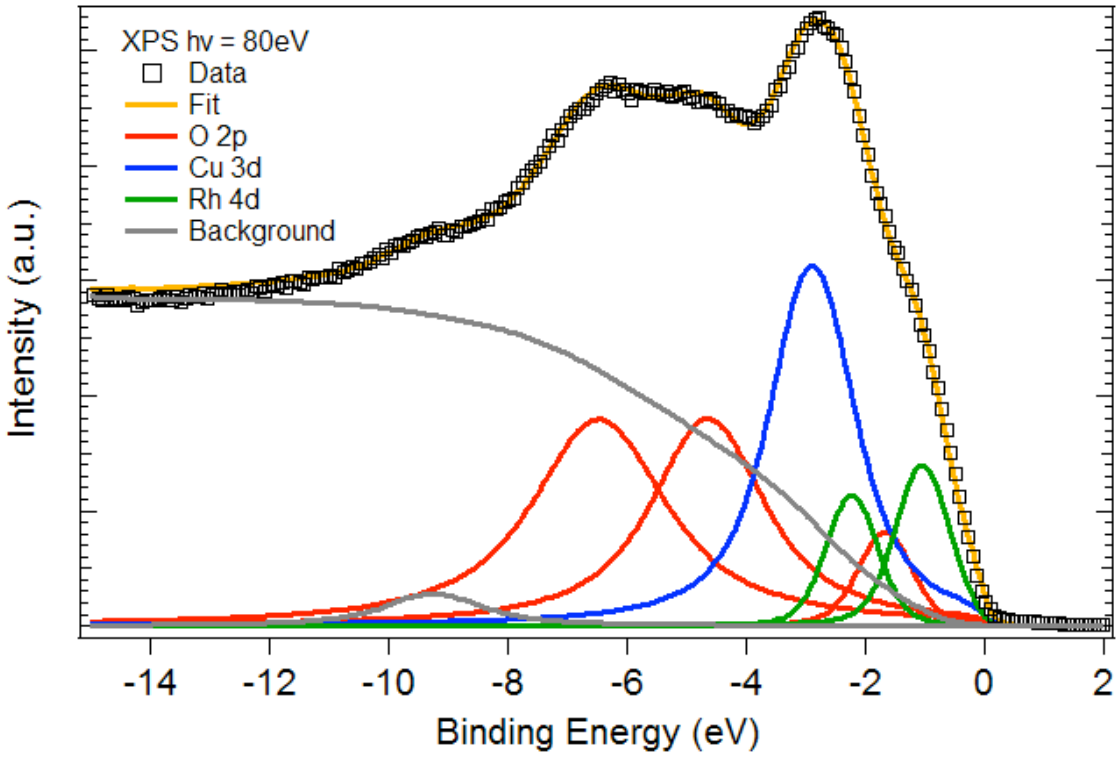

Figure 21. Fitted PES VB spectrum excited by *hv* = 80eV. Red peaks represent O, blue peaks represent Cu, gray curve represents the Shirley background, the gray peak represents a contaminant, and the green peaks at E_F are those that are below confirmed to be Rh.

The fitting procedure has been applied to all spectra while maintaining continuity, and the error has been minimized so that the decomposition is reasonable. From Chapter IV, the differential photoelectron peak intensity dN_k produced by subshell k and originating from volume $dxdydz$ at (x, y, z) has the form:

$$dN_k(\theta) = I_0\,\rho_k(x,y,z)\frac{d\sigma_k}{d\Omega}\Omega(E_{kin})D_o(E_{kin})e^{-z/\Lambda_e \sin\theta}dxdydz, \qquad (1)$$

$\frac{d\sigma_k}{d\Omega}$ = differential photoelectron cross section for peak k,
ρ_k = atomic volume density of peak k,
I_o = intensity of photon flux
Ω = acceptance angle,
D_o = instrumental detection efficiency,

t = thickness of layer,
θ = angle between sample normal and the nose of the analyzer = 50.3°,
Λ_e = inelastic mean free path

In many of the derivations of the total photoelectron peak intensity, the samples are assumed to be homogenous. This is very rarely the case in real sample, but for large electron mean free paths, it is reasonable to assume homogeneity. However, the kinetic energies of the photoelectrons measured in the VB with hv between 60 and 200eV correspond to low Λ_e. Since these samples are layered, the density function $\rho_k(z)$ is defined for each layer as an alternating 0 and constant ρ_k. The integral is converted to a summation over layers in the z direction:

$$\begin{aligned} N_k(\theta) &= I_0 \frac{d\sigma_k}{d\Omega}\Omega(E_{kin})D_o(E_{kin})\frac{A_o(E_{kin})}{\sin\theta}\int_0^\infty \rho_k(z)e^{-z/\Lambda_e \sin\theta}dz \\ &= I_0 \frac{d\sigma_k}{d\Omega}\Omega(E_{kin})D_o(E_{kin})A_o(E_{kin})\Lambda_e(E_{kin})\sum_{i=0}^{\infty}\rho_k\left(\frac{2ci}{\sin\theta}\right)e^{\frac{-2ci}{\Lambda_e \sin\theta}}, \end{aligned} \tag{2}$$

where c is the lattice constant that defines the thickness of each layer, which is about 17.1Å in the $CuRhO_2$ crystals. The above summation applies to the constituents whose first layer is the top layer. For constituents in the next layer, the counting must begin at a depth of $a/\sin\theta$. As before, matters are greatly simplified by comparison of intensities. The elements that are compared in the Rh analysis all have binding energies less than 10eV, and thus their photoelectrons all have energies approximately equal to hv. If Rh is assumed to be the top layer (though both are checked), the ratio of Rh to Cu is:

$$\frac{N_{Rh}}{N_{Cu}} = \frac{\rho_{Rh}\frac{d\sigma_{Rh}}{d\Omega}}{\rho_{Cu}\frac{d\sigma_{Cu}}{d\Omega}} \times \left[\frac{1+e^{\frac{-2a}{\Lambda_e \sin\theta}}+\ldots}{e^{\frac{-a}{\Lambda_e \sin\theta}}+e^{\frac{-3a}{\Lambda_e \sin\theta}}+\ldots}\right] \approx \frac{\rho_{Rh}\frac{d\sigma_{Rh}}{d\Omega}}{\rho_{Cu}\frac{d\sigma_{Cu}}{d\Omega}} \times e^{\frac{a}{\Lambda_e \sin\theta}} \tag{3}$$

Though just a constant scaling factor, for $CuRhO_2$ one may approximate that $\rho_{Rh} \approx 0.9\ \rho_{Cu}$. The calculated photoemission cross sections are plotted in Figure 17. The scaling factor is dependent on Λ_e, which can be approximately calculated using the universal curve given by equation (6) in Chapter IV. Since these photoelectrons are coming from the VB, their kinetic energies are about equal to the excitation photon energies. Lastly, the measured intensity of an orbital is the total contribution of the orbital to the spectrum. Given that the photon energy dependent spectra have been decomposed, the intensities are determined by integrating under all constituent peaks.

To determine the peaks at E_F, their area is compared to area of the peak corresponding to Cu and scaled with the mean free path term in equation (3). These ratios are then compared to the ratio of Rh *4d* to Cu *3d* cross sections. This emphasizes that those states at E_F are Rh-derived.

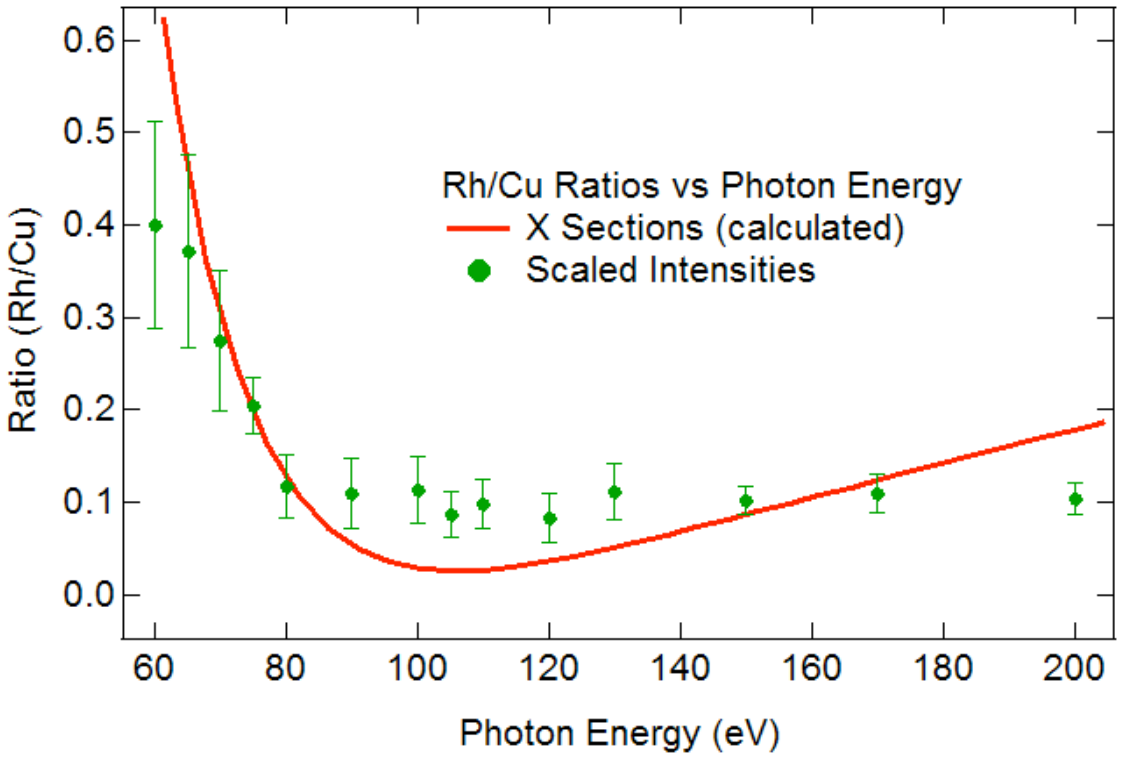

Figure 22. Intensities ratio of Rh to Cu follows the photon energy dependent trend of their cross section ratios.

Conclusion

In summary, the states at E_F in Mg doped $CuRhO_2$ have been determined to be Rh. The presence of Rh at E_F has been verified by exploiting the dichroic nature of the covalently bonded Rh electrons, RPES, and by exploiting the photon energy dependent cross section of the outer Rh *4d* orbital. This lends credence to the relevance of the d^6 orbital states to high thermopower in thermoelectric oxides and encourages further theoretical study of the degenerate states introduced by the d^6 ion in oxides.

CHAPTER VII

CONCLUSIONS AND RECOMMENDATIONS

Soft x-ray spectroscopic techniques are powerful tools for studying the electronic structures of condensed matter systems. These techniques are particularly relevant for the study of materials for energy as they are intended for the study of electrons and holes, the charge carrying particles responsible for the majority of our energy transport. In these projects, several photoemission techniques and x-ray emission have been used to study oxides for the conversions of heat and sunlight into energy.

The intention of the photoemission study of the photovoltaic titanium dioxide (TiO_2) has been to experimentally confirm or deny the application of an intended doping scheme to a new set of crystals. It is known that doping TiO_2 crystals with nitrogen (N) leads to the photovoltaic's absorption of more light in the visible spectrum, and thus a higher efficiency for solar applications. A major problem has been the low solubility of N in TiO_2, which has led researchers to study new ways of incorporating N. One proposed solution has been a doping scheme, termed non-compensated doping, in which equal concentrations of chromium (Cr) and N are introduced into the sample. Samples have been grown using PLD with the suggested nominally non-compensated growth scheme. In this project, these samples have been studied with photoemission, and this nominal growth scheme has been rejected. The realized ratio of the Cr and N compositions has been found to actually be approximately 1.99. However, this project does not entirely reject the new doping scheme for the more efficient introduction of N to TiO_2. Having studied both N only doped samples and codoped (Cr and N) samples, the photoemission

data offer conclusive confirmation that the presence of Cr does encourage the efficient substitution of N for O in TiO_2.

Given the potential impact of TiO_2 photovoltaics, their further study is very recommended. An appropriate next step is for new materials of varying dopant concentrations to be grown with Molecular Beam Epitaxy (MBE), currently the most advanced growth technique for synthesizing artificially-structured single-crystalline films with atomically precise control of thickness and composition. The non-equilibrium synthesis of MBE is likely to produce a variety of different kinetic pathways for dopant incorporation. The synthesis of high-quality materials is also promising for maximization of carrier mobility which, being a property that depends sensitively on the quality of the materials, can be limited by defects that often act as charge traps. To better understand the methods of doping, photoemission (PES) should be applied to all new materials to provide the dopant concentrations, and this should be compared with the nominal concentration of dopants. The quality of the synthesized samples may be tested by photoconductivity and photoluminescence. A comprehensive study of a variety of doping schemes and techniques on TiO_2 has the potential to lead to an ideal scheme and establish a foundation for the microscopic understanding of doping mechanisms. Combining this body of data with information on the solid solubility will narrow down the parameter space where one can search for samples that may become showcases for the codoping scheme.

In the thermoelectric magnesium (Mg) doped copper rhodium oxide ($CuRhO_2$) the states at E_F have been determined to be Rh. The presence of Rh at E_F has been verified by exploiting the dichroic nature of the covalently bonded Rh electrons, RPES, and by exploiting the photon energy dependent cross section of the outer Rh *4d* orbital. This supports theories that relate the high thermopower in thermoelectric oxides to the d^6 orbital states of Co and Rh.

An appropriate next step is to study the dependence of Mg doping on the thermoelectric properties of $CuRhO_2$. The introduction of Mg induces an insulator to metal transition that lead to a tremendous increase in the power factor, as evident in Figure 4. This must be further understood. The crystals studied thus far have been doped such that their stoichiometry is described by $CuRh_{0.9}Mg_{0.1}O_2$. The comparison of the electronic structure of samples with other Mg doping could be very insightful. Additionally such comparison may be useful for determining the contribution of Mg to the valence band.

LIST OF REFERENCES

1. Green MA. Third generation photovoltaics: solar cells for 2020 and beyond. Physica E: Low-dimensional Systems and Nanostructures. 2002; 14(1-2): 65-70.
2. Chen, A. Cool Colors Project: Improved Materials for Cooler Roofs. Environmental Energy Technology Division News. 2004 [cited 2012 April 28]; 5(4). Available from: http://eetd.lbl.gov/newsletter/nl19/.
3. Hoffmann MR, Martin ST, Choi W, Bahnemann DW. Environmental applications of semiconductor photocatalysis. Chemical Review. 1995; 95: 69-96.
4. Grätzel, M. Photoelectrochemical cells. Nature. 2001; 414: 338-344.
5. Fujishima A, Rao TN, Tryk DA. Titanium Dioxide Photocatalysis. Journal of Photochemistry and Photobiology C: Photochemistry. 2000; 1: 1-21.
6. Fujishima A, Honda K. Electrochemical photolysis of water at a semiconductor electrode. Nature. 1972; 238: 37-38.
7. Asahi R, Morikawa T, Ohwaki T, Aoki K, Taga Y. Visible-light photocatalysis in nitrogen-doped titanium oxides. Science. 2001; 294: 269-271.
8. Seery, M. Metal Oxide Photocatalysis. The Photochemistry Portal [Internet]. 2012 [cited 2012 April 28]. Available from: http://photochemistryportal.net/home/index.php/category/semi-conductor-photocatalysis/.
9. Di Valentin C, Diebold U, Selloni A. Doping and functionalization of photoactive semiconducting metal oxides. Chemical Physics. 2008; 339: vii-viii.
10. Koshibae W, Maekawa S. Effects of spin and orbital degeneracy on the thermopower of strongly correlated systems. Physical Review Letters. 2001; 87: 236603(1-4).

11. Okada S, Terasaki, I. Physical properties of Bi-based rhodium oxides with RhO_2 hexagonal layers. Japanese Journal of Applied Physics. 2005; 44: 1834-1837.

12. Okamoto Y, Nohara M, Sakai F, Takagi H. Correlated metallic phase in a doped band insulator $Sr_{1-x}Rh_2O_4$. Journal of the Physical Society of Japan. 2006; 75: 023704(1-4).

13. Maignan A, Volker E, Martin C, Kremer S, Frésard R, Pelloquin D. Electronic structure and thermoelectric properties of $CuRh_{1-x}Mg_xO_2$. Physical Review B. 2009; 80: 115103(1-9).

14. Fujita K, Mochida T, Nakamura K. High-temperature thermoelectric properties of $Na_xCoO_{2-\delta}$ single crystals. Japanese Journal of Applied Physics. 2001; 40: 4464-4647.

15. Klient Ch, Bonzel HP. On the History of Photoemission. Progress in Surface Science. 1995; 49(2): 107-153.

16. Moulder JF, Stickle WF, Sobol PE, Bomben KD. Handbook of X-ray Photoelectron Spectroscopy. Eden Prairie, MN: Perkin-Elmer Corp.; 1995. p 9-28.

17. Diagram courtesy of Norman Mannella.

18. Vilmercati P, Cvetko D, Cossaro A, Morgante A. Heterostructured organic interfaces probed by resonant photoemission. Surface Science. 2009; 604: 1542-1556.

19. Lunney, J. Pulsed laser deposition of metal and metal multilayer films. Applied Surface Science. 1995; 86: 79-85.

20. Omicron Nanotechnology. EA 125 Energy Analyzer User's Guide. Ver. 2.1. 2002.

21. CASA XPS. Peak Fitting in XPS. Casa Software Ltd; 2006. p 5-8.

22. Tougaard S. Quantitative XPS: non-destructive analysis of surface nano-structures. Applied Surface Science. 1996; 100-101: 1-10.

23. Aronniemi M, Sainio J, Lahtinen J. Chemical state quantification of iron and the chromium oxides using XPS: the effect of the background subtraction method. Surface Science. 2005; 578(1-3): 108-123.

24. Castle JE, Salvi AM. Interpretation of the Shirley background. Journal of Vacuum Science and Technology A. 2001; 19(4): 1170-1175.

25. Eisberg R, Resnick R. Quantum Physics of Atoms, Molecules, Solids, Nuclei, and Particles. 2nd Ed. New York: John Wiley & Sons, Inc; 1986. p 278-284.

26. Merzbacher, E. Quantum Mechanics. 3rd Ed. New York: John Wiley & Sons, Inc; 1998. p 502-509.

27. Bohm A, Harshman NL, Walther H. Relating the Lorentzian and exponential: Fermi's approximation, the Fourier transform, and causality. Physics Review A. 2002; 66: 1-11.

28. Fadley CS. Basic Concepts of X-ray Photoelectron Spectroscopy. In: Brundle CR, Baker AD, editors. Electron Spectroscopy: Theory, Techniques and Applications. v 2. London, New York, San Francisco: Academic Press; 1978. p 1-156.

29. Yeh JJ, Lindau I. Atomic Subshell Photoionization Cross Sections and Asymmetry Parameters: $1 \leq Z \leq 103$. Atomic Data and Nuclear Data Tables. 1985; 32: 1-155.

30. Mannella, N. Experimental Methods. In: Soft X-ray Spectroscopic and Structural Studies of Strongly Correlated Oxides [dissertation]. Davis, CA: University of California Davis; 2003.

31. Band IM, Kharitonov YI, Trzhaskovskaya MB. Photoionization cross sections and photoelectron angular distributions for x-ray line energies in the range 0.132-4.509 keV targets: $1 \leq Z \leq 100$. Atomic Data and Nuclear Data Tables. 1979; 23: 443-505.

32. Hüfner S. Photoelectron Spectroscopy: Principles and Applications. Springer Series in Solid-State Sciences. 1995; 82.

33. Seah MP, Dench WA. Quantitative Electron Spectroscopy of Surfaces: A Standard Data Base for Electron Inelastic Mean Free Paths in Solids. Surface and Interface Analysis. 1979; 1: 2.

34. Terasaki I, Sasago Y, Uchinokura K. Large thermoelectric power in $NaCo_2O_4$ single crystals. Physical Review B. 1997; 56(20): 685-687.

35. Shibasaki S, Kobayashi W, Terasaki I. Transport properties of the delafossite Rh oxide $Cu_{1-x}Ag_xRh_{1-y}Mg_yO_2$: Effect of Mg substitution on the resistivity and Hall coefficient. Physical Review B. 2006; 74: 235110(1-6).